Chapter 1

IMAGE-DRIVEN COMPUTATIONAL MODELS OF THE HEART FOR TETRALOGY OF FALLOT

Tommaso Mansi, [*] ***Xavier Pennec, Maxime Sermesant, Hervé Delingette and Nicholas Ayache***
Asclepios Research Team, INRIA Sophia Antipolis - Méditerranée, France

Keywords: Myocardium Strain Estimation; Heart Remodelling; Myocardium Electromechanics; Personalised Therapy Simulation; Tetralogy of Fallot.

Abstract

In the last decades, researchers have been striving to develop computational models of the beating heart. Shifting from model generality to patient specificity, recent studies are demonstrating the potential impacts of such models on the clinical workflow. This chapter introduces three image-driven computational models of the heart that combine statistical and physiological priors for diagnosis, prognosis and therapy planning in repaired tetralogy of Fallot (rToF), a severe congenital heart disease. We first illustrate how physiological priors about the cardiac mechanics make the estimation of myocardium strain more reliable, thus improving disease diagnosis. An algorithm that automatically tracks the heart along image sequences is constrained to estimate elastic and incompressible deformations, two fundamental properties of the myocardium. Then, we estimate a generative model of the right ventricular (RV) remodelling in rToF patients for disease prognosis. Computed using statistical shape analyses and partial least squares, the model suggested that the dilation, the basal bulging and the apical dilation typically observed in these patients appear progressively as the child grows. These findings could support the cardiologist in predicting the evolution of the pathology for planning pulmonary valve replacement (PVR), the current state-of-the-art therapy in rToF. Finally, we introduce an electromechanical (EM) model of the heart for personalised planning of PVR with RV volume reduction in two patients. The EM model simulates the main features of the beating heart. After personalisation, the virtual heart is used to simulate PVR. As expected, the predicted postoperative function significantly improved in both patients. As illustrated by these results, combining medical

[*]E-mail address: thomas_mansi@yahoo.fr

imaging and computational models of the heart can thus provide a powerful framework for a computer-assisted medicine.

1. Introduction

Diagnosis, prognosis, therapy planning, three steps of the clinical workflow that are greatly challenged by chronic diseases, like congenital heart defects (CHD). CHD involve severe anatomical and functional abnormalities of the heart, which often require surgical repair early in infancy. In some cases, that initial repair yields sequels that, although initially asymptomatic, can become life-threatening decades after the intervention. The wide time-scale of CHD and the large variability in child growth and disease evolution greatly challenges the clinical management of these patients. Repeated long-term follow-ups are therefore necessary and re-intervention may be required. A question arises in light of these difficulties. Can computational models of the heart assist the cardiologists in the clinical workflow of CHD?

The last decades have seen advances in medical image processing, organ shape analysis, and physiological modelling of the cardiac function. Medical image analysis is providing efficient and non-invasive tools to quantify the cardiac anatomy and function. In parallel, recent well-posed mathematical frameworks enable one to quantitatively study organ shapes. Finally, researchers are striving to develop detailed biophysical models of the heart to understand its mechanisms.

One can imagine how much those tools can impact the clinical workflow. On the one hand, they can help in interpreting clinical data, extracting more discriminative features, thus improving diagnosis. On the other hand, models can be personalised from clinical data to reproduce the patient physiology. It would then be possible to predict the evolution of a pathology and to test therapies, thus facilitating patient management and therapy planning. Nevertheless, translating these tools to the clinics is challenged by the sparsity of the clinical data, especially in paediatrics. Models often depend on parameters that are difficult to estimate from standard clinical data. Trade-offs have to be done between model accuracy and parameter observability.

This chapter presents recent advances in image-driven models of the heart for paediatrics, with particular focus on repaired tetralogy of Fallot (rToF). ToF is a severe CHD of the right ventricle (RV) and the pulmonary artery that requires early intervention. Although that initial repair has nowadays very low mortality and morbidity [20], it often damages the pulmonary valves, resulting in blood leakage from the pulmonary artery to the RV, the so-called pulmonary regurgitation. In the long-term, the chronic regurgitation makes the RV dilate and deform (Fig. 1). The cardiac function weakens and the probability of sudden death increases tremendously [83]. Nowadays, it is acknowledged that replacing the valves significantly increases the life expectancy of these patients [99]. The challenge though is to determine the right timing for pulmonary valve replacement (PVR). Early PVR can lead to repeated re-intervention due to heart growth and limited valve lifespan. Conversely, late PVR may be inefficient due to irreversible damage of the RV [99]. High variability in pathology course and in RV anatomy makes difficult the decision of optimal timing [34,98]. Metrics that quantify the cardiac deformation could provide a more comprehensive view of the myocardium integrity. Yet, this task is challenging in paediatrics as only standard

anatomical images of the beating heart are usually available. In fact, ideally one would want to predict if the heart will deteriorate in the near future, which is difficult due to the long-term nature of the disease (measured in decades). Finally, at the time of intervention, the cardiologist must choose between several PVR techniques [23, 46], whose postoperative outcomes can vary from one patient to another. It is therefore necessary to predict the outcomes of each of these therapies on the patient cardiac function.

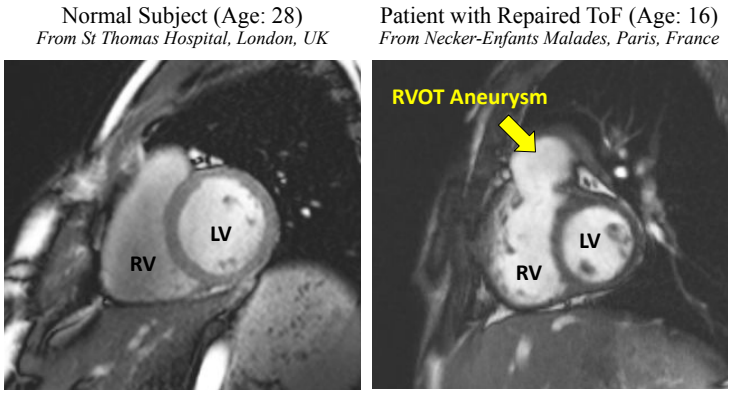


Figure 1. *Left panel*: MRI of a normal heart. *Right panel*: MRI of a patient with repaired tetralogy of Fallot (rToF). Observe the dilated right ventricle (RV) compared to the left ventricle (LV) in rToF, and the aneurysm at the RV outflow tract due to the corrective patch.

We present in this chapter three image-driven models of the heart that aim to assist the clinical management of rToF patients. We first introduce an image-based algorithm that enables one to estimate myocardium strain from standard anatomical images of the beating heart (Sec. 2.). The idea is to rely on fundamental properties of the myocardium, namely elasticity and incompressibility, to make the estimation of the cardiac strain more reliable when images suffer from low quality, as in cine MRI for instance. Results on an rToF patient supported our approach. Second, we present a statistical model of RV growth and remodelling in rToF that quantifies the pathological changes of the RV morphology (Sec. 3.). Statistical analyses of shape and cross-sectional designs are combined together to estimate a first generative model of the RV growth. Exhibited trends were found realistic by cardiologists and were consistent with observations reported in the clinical literature. Finally, an electromechanical model of the beating heart for PVR simulation is described (Sec. 4.). This model is adapted to the specificities of rToF and personalised from patient data. The resulting virtual heart is then used to predict the postoperative outcomes of surgical PVR with RV volume reduction [23]. Tested on two patients, the model showed that both left ventricle (LV) and RV function are improved by the intervention.

2. Quantifying Cardiac Deformation from Images

2.1. Background

Analysing the cardiac motion can provide crucial insights into the heart condition. Nowadays, tagged magnetic resonance images (MRI) [53, 108] and DENSE MRI [3, 28] are

considered the gold standard for myocardium motion assessment although they are seldom available in clinical routine. Alternatively, ultrasound 2D speckle tracking, or 2D strain [97], is widely available in the clinical setup despite the facts it is two-dimensional and it suffers from high inter-rater variability [18]. Estimating myocardium strain from gated cine MRI (cMRI) constitutes an attractive choice. cMRI is standard, even in paediatrics, and provides detailed images of the beating heart. However, accurately estimating the 3D motion from these images is challenged by the large slice thickness ($\approx 10\,mm$) and the lack of consistent texture within the myocardium. Prior knowledge about cardiac dynamics is thus required.

Regardless of the challenges, various methods have been proposed to estimate myocardium deformation from cMRI. The common idea is to track the myocardium along the image sequences using image registration. Some approaches enhance the tracking with a biomechanical model of the myocardium [66,82,104], yielding promising results. However, those models may not apply anymore in diseased hearts and their parameters may be difficult to determine *in-vivo*. Purely image-driven methods have thus been proposed, relying on temporal constraints [24] or manual segmentations [29]. But contrary to model-based tracking, these approaches may yield deformations inconsistent with heart biomechanics. During the cardiac cycle, the volume of the myocardium varies by less than 5% [35]. It is therefore reasonable to enforce incompressibility when estimating the cardiac motion, as this property is true for diseased hearts as well. This idea was explored by Bistoquet *et al.* [12]. They obtained promising results despite the fact they relied on a first order approximation of the incompressibility constraint, which does not hold for the large displacements the heart undergoes during systole.

This section describes an image registration algorithm suitable for myocardium strain estimation on clinical cMRI. Our approach relies on log-domain diffeomorphic demons [102], henceforth termed logDemons, an efficient non-linear registration algorithm that estimates smooth, one-to-one mapping between two images. The algorithm is constrained to provide incompressible and elastic deformations. Incompressibility constraints have been used in the past on contrast-enhanced images [38, 76, 78], and recently in heart tracking [12, 105]. However, they are often obtained through *ad-hoc* and computationally demanding numerical schemes. Here, we present a well-posed and simple approach that constrains the parameters of the diffeomorphisms. Myocardium elasticity is implemented using an elastic-like kernel regularisation [15], which guarantees smooth strain maps. The Lagrangian finite strain tensor is finally calculated from the recovered deformations. The method is illustrated on a rToF patient. The reader is referred to [51] for the mathematical developments and more quantitative comparisons with tMRI in adults with heart failure.

2.2. Physiologically-Constrained Image Registration Method

2.2.1. Efficient Diffeomorphic Image Registration with Log-Domain Demons

Non-linear image registration estimates a transformation $\phi = \mathrm{Id} + \mathbf{u}$, $\mathbf{u}$ is a displacement field, which best aligns a template image T with a reference image R [56]. This is usually achieved by minimising an energy functional $\mathcal{E}(\phi)$ that comprises a similarity criterion $\mathcal{D}(R, T \circ \phi)$, which measures how similar the images R and $T \circ \phi$ are, and a regulariser $\mathcal{R}(\phi)$, which integrates prior knowledge about the deformation and ensures its smoothness.

The logDemons algorithm [102] is an efficient image registration method that estimates a diffeomorphic deformation ϕ defined in the Log-Euclidian framework [7]. ϕ is uniquely parameterised by a stationary velocity field $\mathbf{v}$ through the exponential map $\phi = \exp(\mathbf{v})$. The algorithm estimates ϕ by iterating two alternate steps. Assume a current estimate of ϕ is given (the identity transformation for instance). First, ϕ is updated according to the diffeomorphic update rule, $\phi \leftarrow \phi \circ \exp(\delta\mathbf{v})$, where $\delta\mathbf{v}$ is a small update velocity. Vercauteren *et al.* demonstrated that $\delta\mathbf{v}$ has a closed form at every voxel of the image domain $\Omega \subset \mathbb{R}^3$, $\delta\mathbf{v} = -(R - T \circ \phi)/(\|J\|^2 + \lambda_i^2/\lambda_x^2)$, $J = 1/2[\nabla R + \nabla(T \circ \phi)]$ [103]. Next, a Gaussian smoothing is applied on the updated field to ensure deformation smoothness. The two steps are performed entirely in the log-domain of velocities, until convergence.

2.2.2. Integration of Cardiac Elasticity Constraint

In [51], we demonstrated that logDemons Gaussian regularisation models a diffusion process, which is not compatible with the elastic cardiac deformation [35]. We thus need to modify the regularisation such that the estimated deformations are elastic. Linear elastic regularisers have been proposed [14, 56] but they are suitable for small displacements only and can yield non-smooth strains. To overcome these limitations, we instead regularise the deformation field using an elastic-like separable vector filter $G_{\sigma,\kappa} = G_\sigma \mathrm{Id} + \sigma\kappa/(\kappa+1)\mathcal{H}G_\sigma$ [15]. G_σ is the Gaussian kernel of standard deviation σ, $\mathcal{H}G_\sigma$ is its Hessian, and κ is a parameter that behaves like the Poisson ratio. The higher is κ, the stiffer is the deformation. This filter is mathematically justified in the logDemons algorithm using isotropic differential quadratic forms [15, 51].

2.2.3. Integration of Cardiac Near-Incompressibility Constraint

One can demonstrate that deformations parameterised by divergence-free stationary velocity fields are incompressible [27]. We thus constrain the logDemons algorithm to estimate incompressible deformations by searching for the optimal velocity $\mathbf{v}$ in the space of divergence-free vector field W. This is achieved by projecting the smoothed velocity $\mathbf{v}$ onto W using the Helmholtz decomposition [51, 93], $\mathbf{v}_{div-free} = G_{\sigma,\kappa} \star \mathbf{v} - \nabla p$. In that equation, p is the solution to the Poisson equation $\Delta p = -\nabla \cdot (G_{\sigma,\kappa} \star \mathbf{v})$ under 0-Dirichlet boundary conditions typically defined at the myocardium wall.

Algorithm 1 summarises the main steps of the proposed incompressible elastic logDemons, called *iLogDemons* in the following.

2.2.4. Estimation of Myocardium Strain

Myocardium strain is estimated by tracking the heart recursively along the image sequence. Elasticity is enabled and incompressibility is ensured only within the myocardium (Fig. 2, left panel). Let I_0 be the reference frame at end-diastole. The strain between the images I_0 and $I_{k>0}$ is computed from the deformation that registers $I_{k>0}$ to I_0. A recursive strategy is employed to take advantage of the frame-by-frame registration accuracy while minimising tracking errors due to the changing appearance of the trabecula, papillary muscles and neighbouring organs. Let the spatial transformation $\phi_{I_{k-1} \to I_0}$ be known. We first perform

Algorithm 1 iLogDemons: Incompressible Elastic-Like LogDemons Registration

Require: Stationary velocity field $\mathbf{v}^0$. {Usually $\mathbf{v}^0 = \mathbf{0}$ i.e. $\phi^0 = \mathrm{Id}$}.

1: **loop** {*over n until convergence*}
2: Compute the update velocity: $\delta\mathbf{v}^n$ given $\mathbf{v}^{n-1}$.
3: Optional fluid-like regularisation: $\delta\mathbf{v}^n \leftarrow G_{\sigma_{fl}} \star \delta\mathbf{v}^n$, $G_{\sigma_{fl}}$ is a Gaussian kernel to ensure numerical stability.
4: Update the correspondence velocity: $\mathbf{v}^n \leftarrow \mathbf{v}^{n-1} + \delta\mathbf{v}^n$ (0^{th}-order Baker-Campbell-Hausdorff composition [102].
5: Elastic-like regularisation: $\mathbf{v}^n \leftarrow G_{\sigma,\kappa} \star \mathbf{v}^n$
6: Solve: $\Delta p = \nabla \cdot \mathbf{v}^n$ with 0-Dirichlet boundary conditions
7: Project the velocity field: $\mathbf{v}^n \leftarrow \mathbf{v}^n - \nabla p$.
8: **end loop**
9: **return** $\mathbf{v}$, $\phi = \exp(\mathbf{v})$ and $\phi^{-1} = \exp(-\mathbf{v})$.

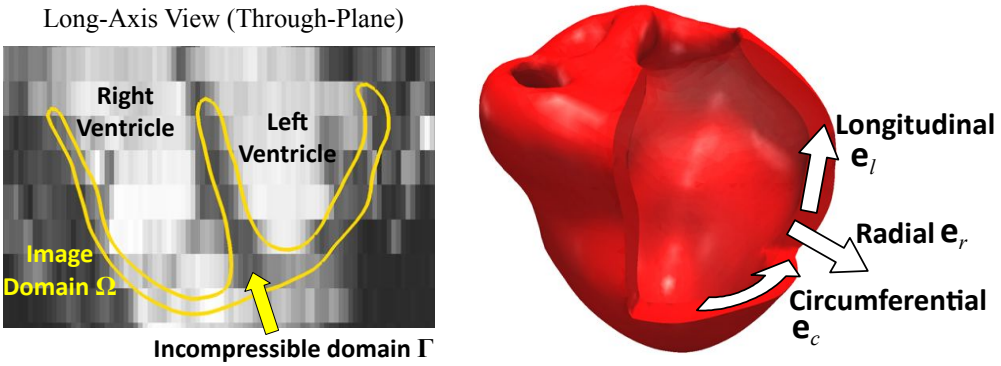


Figure 2. *Left panel*: Short-axis cMRI of an rToF patient (*Necker Enfants Malades, Paris, France*). Incompressibility is ensured only within the myocardium (outlined in yellow). Note the coarse through plane resolution. *Right panel*: Local prolate coordinate system.

a frame-by-frame registration $\phi_{I_k \to I_{k-1}}$. We then estimate the transformation $\phi_{I_k \to I_0}$ by taking as initialisation the composed transformation $\phi_{I_k \to I_{k-1}} \circ \phi_{I_{k-1} \to I_0}$. The Lagrangian finite strain tensor $\mathrm{E} = 1/2(\nabla\mathbf{u} + \nabla\mathbf{u}^T + \nabla\mathbf{u}^T\nabla\mathbf{u})$ is computed from the estimated displacements $\mathbf{u}$. Radial, circumferential and longitudinal strains are calculated by projecting E onto the local prolate coordinate system (e_r, e_c, e_l) defined in [57] (Fig. 2, right panel)

2.3. Result on a Patient with Repaired Tetralogy of Fallot

The method was tested on a 10-year old rToF patient. Steady-State Free Precession (SSFP) cMRI of the heart were acquired in the short-axis view covering the entirety of both ventricles (10 9.6mm-thick slices; $1.02 \times 1.02\,mm^2$ in-plane resolution; 25 time frames, 1.5T MR scanner, Avanto, Siemens Medical Systems, Erlangen, Germany). No longitudinal cMRI were available. Visual inspection of the images revealed no slice misalignment. Circumferential 2D-strain measurements were performed in the short-axis view (80 frames per second) using Automatic Functional Imaging (AFI, Vivid7, General Electrics, Vingmed

Ultrasound). The heart was tracked on the cMRI using both logDemons and iLogDemons. Registration parameters were set to standard values: $\lambda_x = 1$, $\sigma^2 = 2$, $\sigma^2_{fl} = 0.5$, and $\kappa = 1$. A 2-level multi-resolution scheme was used and the registration was automatically stopped at convergence. We refer the reader to [51] for a more comprehensive analysis of those parameters.

Results are reported in Fig. 3. Despite the different nature of the measurements (cMRI is 3D, 2D-strain is 2D), the circumferential strains estimated on cMRI by the iLogDemons exhibited similar variation patterns as those measured by AFI, with similar amplitudes. In particular, iLogDemons was able to capture the abnormal motion of the anterior region (cyan curve). Interestingly, logDemons algorithm, i.e. without any constraint, over estimated the deformations, with wrong positive strains. The priors about the cardiac motion helped the recovery of the cardiac motion. We recall however that 2D-strain measurements only provide a 2D view of the cardiac deformation and are prone to rater variability [18], contrary to our method, which automatically computes 3D strains in a 3D volume.

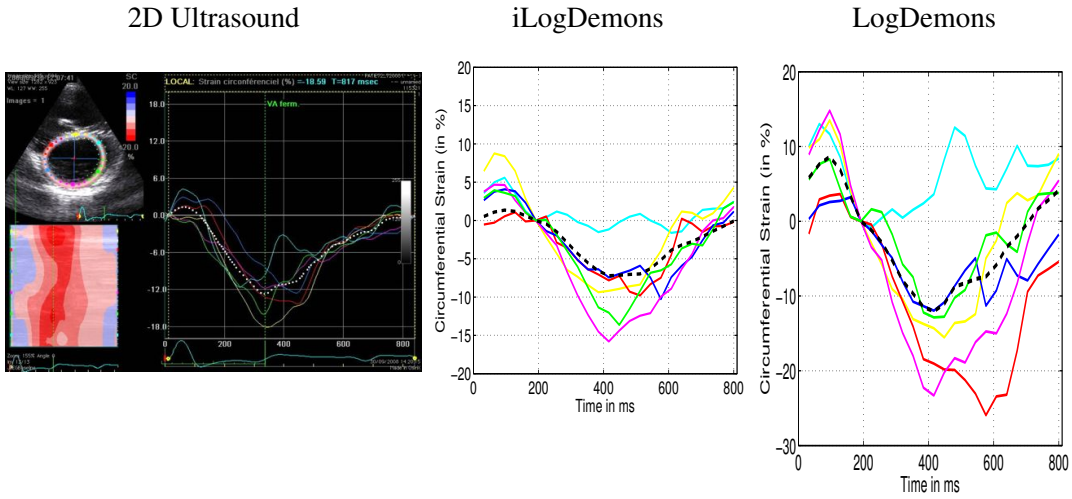


Figure 3. Circumferential strain in an rToF patient (*Necker Enfants Malades, Paris, France*). *Left panel*: 2D-strain measurement. *Mid panel*: estimation on cMRI with iLogDemons. *Right panel*: estimation on cMRI with logDemons. Colours correspond to the same myocardium regions. Contrary to logDemons, iLogDemons recovered more realistic strains.

2.4. Discussion

Guiding an image-based registration algorithm with physiological priors about the cardiac function can significantly improve the accuracy of the estimated displacements. We applied this principle to the logDemons algorithm. We rigorously integrated elasticity and incompressibility into the algorithm, which yielded a significant improvement in the estimation of myocardium strain. Elasticity was modelled through a separable elastic-like vector filter. Incompressibility was ensured by parameterising the deformations with divergence-free velocity fields. The two constraints are linear, they are easy to implement and they can be

disabled by the user easily as they do not require any *ad-hoc* numerical scheme.

In [51], we showed that iLogDemons algorithm can estimate realistic radial, circumferential and longitudinal strains on cMRI of adults with heart failure, which was not possible using the logDemons alone. Here, we applied the algorithm on a young rToF patients, with similar results. In all the cases, the physical constraints reoriented the displacement vectors within the myocardium to satisfy the elasticity and incompressibility assumptions. As a result, circumferential and longitudinal cardiac motion were better captured even if poorly visible in the image.

Future work includes a more thorough validation on larger populations, with quantitative comparisons with tagged MRI or 3D full-volume ultrasound. This method may become a useful tool for cardiac function evaluation and diagnosis.

3. Statistical Model of Right Ventricle Growth and Remodelling

Diagnosing congenital heart defects may not be enough for an optimal management of these patients. In repaired tetralogy of Fallot for instance, anticipating any future heart collapse may greatly support the cardiologist in deciding the optimal timing for PVR. Contrary to the LV, whose morphological alterations are well documented, the complex RV anatomy can vary tremendously among rToF patients. Several studies investigated possible correlations between global clinical features related to the RV morphology [34] but few works have quantified its anatomical changes. In [91], the authors measured the most striking differences in RV shape with respect to normals, quantifying some features of the complex RV remodelling observed in rToF. However, only one-dimensional indices were considered despite the availability of 3D segmentations. In [109], the authors presented a 4D shape model of the heart to segment the RV in cMRI. New shape-based indices were proposed to classify patients from normals but authors did not correlate these indices with clinical features of ToF.

The complexity of cardiac remodelling makes the prediction of the heart shape and function difficult. The large time scale of heart growth hinders modelling the biological mechanisms involved in tissue remodelling. Available models [2, 47, 75] focus on specific aspects only. Recently, well-posed mathematical methods have been developed for studying organ shapes among a population. These methods study how a representative template of a population of shapes deforms within this population [6, 25, 37, 44]. The observed changes may then reveal modifications of the underlying biology. Different approaches are available, varying in the way they estimate the template and the deformations.

Aiming at quantifying the morphological changes along time in rToF patients, we propose to statistically correlate the RV shape with body surface area (BSA), a continuous feature of patient morphology that correlates with age in paediatrics. First, we estimate a representative template of the RV from a cohort of 32 young patients (Sec. 3.1.). Next, we employ partial least-squares regression and canonical correlation analysis to estimate a generative model of RV remodelling (Sec. 3.2.). Finally, the ability of the model to represent the population is tested on seven new patients (Sec 3.3.). The results supported our approach. A realistic RV remodelling model was obtained despite the small number of patients.

3.1. Estimation of a Representative Template of the Right Ventricle

3.1.1. Clinical Data of the Study

32 young rToF patients (19 males) were selected based on their age (from 10 to 30 years, mean $\pm$ SD = 16.1 ± 4.1) and their pulmonary regurgitation fraction (higher than 10%). None of which have under-gone valve replacement. BSA was reported for each patient (mean $\pm$ SD = $1.53 \pm 0.35\, m^2$, correlation with age: $R^2 > 0.5$, $p < 0.001$). SSFP cMRI of the heart were acquired in the short-axis view covering entirely both ventricles (10-15 slices; isotropic in-plane resolution: $1.1 \times 1.1\, mm^2$ to $1.7 \times 1.7\, mm^2$; slice thickness: $5 - 10\, mm$; $25 - 40$ phases, 1.5T MR scanner, Avanto, Siemens, Medical Systems, Erlangen).

We studied the RV shape at end-diastole, when the anatomical features of the pathology are the most evident [91]. The RV endocardium was segmented on the cMRI by fitting an anatomically accurate geometrical model [110]. Manual refinement was done if necessary. To reduce positioning effects in the shape analysis, the 3D RV meshes were rigidly aligned to a common coordinate frame with a standard least square method [9] as mesh correspondence among the segmentations was guaranteed with geometrical resampling in local coordinates (Fig. 4, left panel).

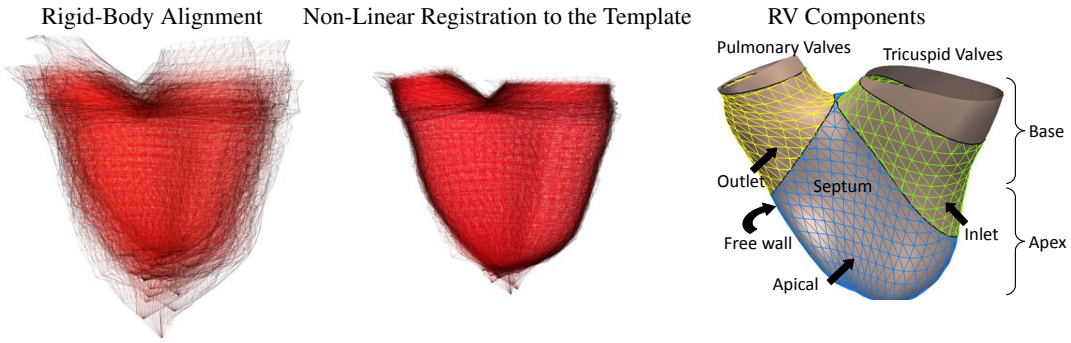


Figure 4. 3D RV meshes of 32 young rToF patients. *Left panel:* The meshes were rigidly aligned to a common coordinate frame. Observe the large variability in RV shape. *Mid panel:* The same meshes registered back to the template using the diffeomorphic non-linear deformations. *Right panel:* Main components of the RV anatomy.

3.1.2. Unbiased Template of the Right Ventricle

The first step of the analysis was to estimate a template that best represents the population. We used the forward model proposed by [25] as 1) the model parameters can be estimated from clinical data; 2) the template and the deformations that match it to the 3D meshes are computed simultaneously and consistently; and 3) it does not require explicit point correspondences.

The observed 3D surfaces $\mathcal{T}^i$ are modelled as the sum of the template $\overline{\mathcal{T}}$, deformed by a diffeomorphic deformation ϕ^i, and a residual term ε^i, which stands for the shape features that cannot be represented by the template nor the deformations (for instance topology changes, acquisition artefacts, etc.). For a given template, the shape information is either in

the deformations or the residual. The shapes, the residuals and the deformations are represented using currents [25, 36], a mathematical framework that does not require mesh point correspondences and that enable statistical operations on shapes. The deformations ϕ^i are computed using the Large Deformation Diffeomorphic Metric Mapping (LDDMM) algorithm on currents [101]. The ϕ^i's are parameterised by smooth initial vector fields $\mathbf{v}_0^i$ that are uniquely defined by moments vectors β^i. Finally, the template $\overline{\mathcal{T}}$ and the deformations ϕ^i are estimated simultaneously with an alternate two-step strategy [25].

The framework is controlled by two parameters. The first one, denoted λ_V, controls the "stiffness" of the non-linear deformations ϕ^i. High values favour more global transformations. As we were mainly interested in the regional changes due to rToF (dilation, valve enlargement, regional bulging), we set $\lambda_V = 30mm$, about the diameter of the pulmonary valve. The second parameter is the resolution of the currents representation, λ_W. It controls the level of shape feature to analyse. In our experiment, we set $\lambda_W = 10mm$ to have good mesh matching while avoiding artefacts due to the large slice thickness of the cMRI.

With these parameters, the estimated RV template was well-centred with respect to the population (standardised mean of velocities, $\nu = mean/sd = 0.2$). Most of the shape variability observed in the population was captured by the deformations (Fig. 4, mid panel). Remaining differences were mainly segmentation artefacts, thus not relevant for the analysis. Interestingly, the age of the closest patient to the template was 16 and his BSA was $1.64m^2$. Both values were close to the population mean, suggesting consistency between the mean shape and these clinical feature.

3.2. A Generative Model of Right Ventricle Growth and Remodelling

3.2.1. Model Dimension Reduction

We analysed the shape information captured by the deformations ϕ^i to investigate the regional changes of the RV anatomy. The residuals were discarded as they may be polluted by the segmentation artefacts common in cMRI. However, applying statistical methods on the ϕ^i's directly was not possible due to the very large dimension of ϕ^i (thousands of parameters). We tackled this issue by projecting the ϕ^i's onto an optimal, low-dimensional subspace that best explained the covariance between shape and BSA. That subspace was automatically computed using partial least squares (PLS) regression [77] on the moments β^i of the deformations. We then selected a subset of q PLS components $\mathbf{b}^m$ and projected the deformations ϕ^i to the spanned subspace, resulting in a unique q-dimensional shape vector $\mathbf{s}^i = \{s_m^i\}_{m=1..q}$, $s_m^i =< \beta^i, \mathbf{b}^m >$ for every patient.

The seven first PLS modes captured 98% of the BSA variability and 66% of the shape variability (Fig. 5). Every patient was thus represented by a seven-dimensional shape vectors $\mathbf{s}^i$. It has to be noted that in that analysis, we were mainly interested in the shape information relevant to BSA and not to the total shape variability.

Linear regression showed a strong correlation between the PLS modes and BSA. The fit was good ($R^2 = 0.85$, $p < 10^{-5}$) and all the PLS modes were found very significant to the linear model ($p < 0.005$). As one can see from Fig. 5, the first mode captured an overall RV dilation. The second mode exhibited a significant bulging of the RV base associated with an aneurysm of the right ventricle outflow tract (RVOT). The third mode showed a more rectangular apex, while the fourth mode captured a positioning of the apex towards

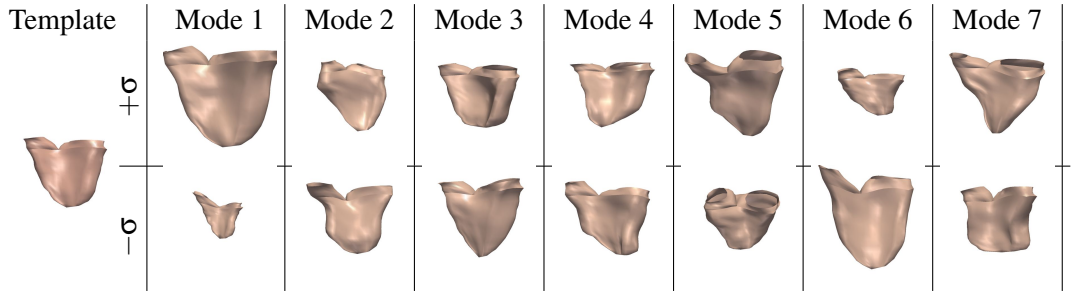


Figure 5. The seven first deformation modes extracted by partial least-squares between RV shape and body surface area (BSA) (32 rToF patients). The modes evolve towards $+\sigma$ when BSA increases.

the pulmonary artery. The fifth and seventh modes clearly captured an elongation of the RVOT which, along with the second mode, may encode the RVOT aneurysm.

3.2.2. Correlation Analysis

Canonical Correlation Analysis (CCA) was then applied between the shape vectors $\mathbf{s}^i$ and BSA to quantify the amount of variation of each PLS mode when BSA varies. CCA is a generalisation of the correlation coefficient to multivariate sets. In our case, CCA tells how much we should walk along each PLS mode when BSA increases. Let R be the overall correlation coefficient between BSA and the shape vectors $\mathbf{s}^i$; and ρ be the correlation vector whose elements relate each PLS mode with BSA. The moment vectors μ of the growth deformation Φ are $\mu = R \sum_k \rho[k]\mathbf{b}^k$. Deforming the template $\overline{T}$ with Φ enables one to quantify the average RV remodelling observed in the population.

Fig. 6 illustrates the RV growth observed in our population. As BSA increased, RV volume increased, the RV free-wall and the valves dilated, and an aneurysm appeared at the RVOT. These patterns were reported in clinical studies based on 1-2D shape features [91] or on RV volumes [13, 34]. The model was found clinically realistic by the cardiologists involved in the study. More quantitatively, the overall correlation coefficient was $R = 0.92$, which confirmed the strong correlation between the PLS modes and BSA.

3.3. Generalisation of the Right Ventricle Growth Model

Generalising the statistical model of RV growth is crucial for disease prognosis. The model must be valid for a wide range of rToF patients. We thus tested the ability of our model to represent seven additional rToF patients with matched ages. Ideally, one would like to predict their RV shape from their BSA. This task is very challenging as it requires transporting the model to the patient space [71, 72]. As an alternative, we estimated patients BSA from their RV shape. Although not meaningful in practice, this approach still enables one to assess the generalisation of the model. The shape vectors $\mathbf{s}$ of each patient was computed as in Sec. 3.2.1. and their BSA was estimated using the linear model learned in Sec. 3.2.1.. The predicted BSA successfully compared with the measured values. The average prediction error ($0.18\,m^2$) was below population SD ($0.35\,m^2$) with a 95% prediction interval of

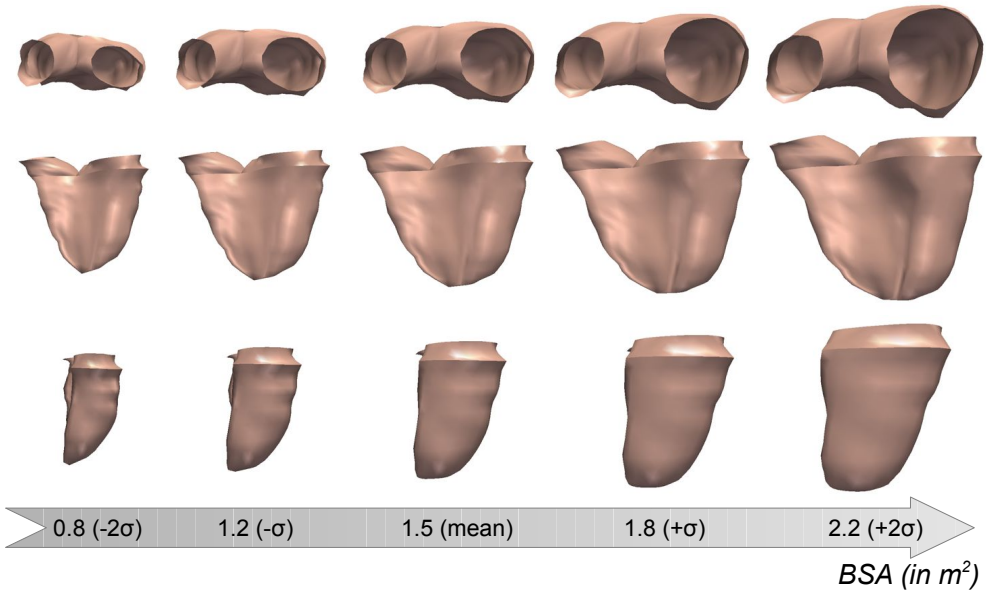


Figure 6. Statistical model of the RV growth observed in a population of 32 ToF patients. When BSA increases, RV globally enlarges, the apex and the valves dilate, and the RV free wall becomes rounder. Later, an aneurysm appears at the right ventricle outflow tract.

$0.35\,m^2$. Our model could fairly well represent the new patients despite the large variability of the RV shape in rToF.

3.4. Discussion

Aiming to quantify and predict the evolution of the RV shape in rToF patients, we modelled the impact of growth upon the end-diastolic RV anatomy from 32 rToF patients. The RV at end-diastole was considered as it is the time when the effects of the pathology are the most evident [91]. The generative model exhibited realistic RV remodelling that was consistent with observations reported in the literature but computed from different clinical features [13, 91]. Interestingly, the model was very similar to the one we previously reported in [50], where only 19 patients were used. This promising consistency further supports our method. To the best of our knowledge, that model constitutes a first attempt at correlating the 3D RV shape with clinical measurements in rToF. Our findings may yield quantitative image-based indices for RV quantification and PVR planning.

As future work, it would be interesting to apply the statistical growth model on a specific patient to predict how its RV will remodel. A promising way to achieve this goal is to use parallel transport [71, 72], which could also be employed to investigate how the 4D cardiac motion is affected by the pathology. More complex models that consider the cardiac biomechanics could also be investigated to strengthen the statistical analyses. A possible direction would be to use manifold learning for instance [39]. From a clinical point of view, one could apply the proposed statistical framework to quantify the impact of the initial repair on the RV remodelling [32, 80], the link between heart remodelling and genomics or

electrophysiology. Understanding these connections may provide new criteria for deciding the optimal timing of PVR. The LV-RV interaction could also be investigated by creating models of the bi-ventricular myocardium. Finally, the approach could also be applied on postoperative data to study the long-term impact of valve implant on the RV anatomy and function.

4. Personalised Simulation of Pulmonary Valve Replacement

Information from pathology assessment, like an impaired cardiac deformation, and prognosis, like a predicted collapse of the heart, may lead the clinician to decide an immediate pulmonary valve replacement (PVR). Several pulmonary valve replacement strategies are currently available but their outcomes greatly depend on the pathophysiology of the patients. A PVR technique may be more appropriate for a patient than another. Is valve replacement alone enough, the heart remodels itself after the intervention? Should one manually reduce the RV and remove lesions, scars and aneurysms [23]? There is nowadays no clinical consensus on that question. Ideally, one would predict the outcome of each strategy on the patient and choose the best one.

In the last decades, computational models of the heart have been proposed to simulate the biological phenomena that govern the cardiac activity, from electrophysiology to biomechanics [40, 43, 52, 61, 79]. Primarily developed to study the organ in general, these models are now being adapted to patient-specific clinical situations [49, 54, 85, 86, 89, 107]. At the same time, platforms are being developed for simulating soft-tissue intervention in real-time [5].

Based on these advances, we propose to use an electromechanical (EM) model of the heart to predict the outcomes of PVR with direct RV volume reduction. The idea is to predict the effects of that therapy on a patient using a personalised computational model of the beating heart [49]. As in [86,107], we had to simplify the model, but without hampering the realism of the simulations, such that its parameters could be estimated from standard clinical data. Recently, Yang et al. [107] performed a similar experience in rToF based on a fluid-structure interaction with a passive model of the myocardium. Presented results were very promising although only a partial view of the cardiac system was obtained as the active properties of the myocardium were discarded. In this chapter, we simulate the effects of the therapy with an active model of the heart.

Fig. 7 illustrates the different steps of our method [49]. The bi-ventricular myocardium

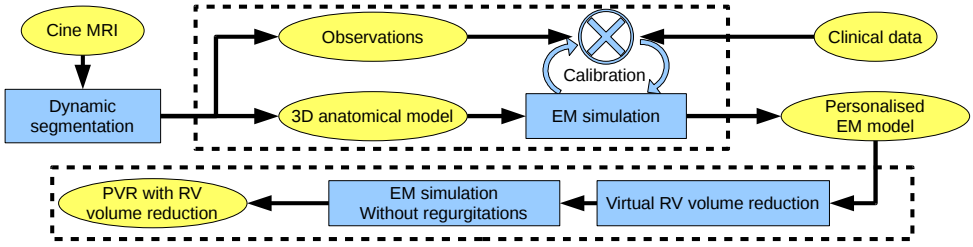


Figure 7. Pipeline for personalised *in-silico* simulation of PVR *(see details in text)*.

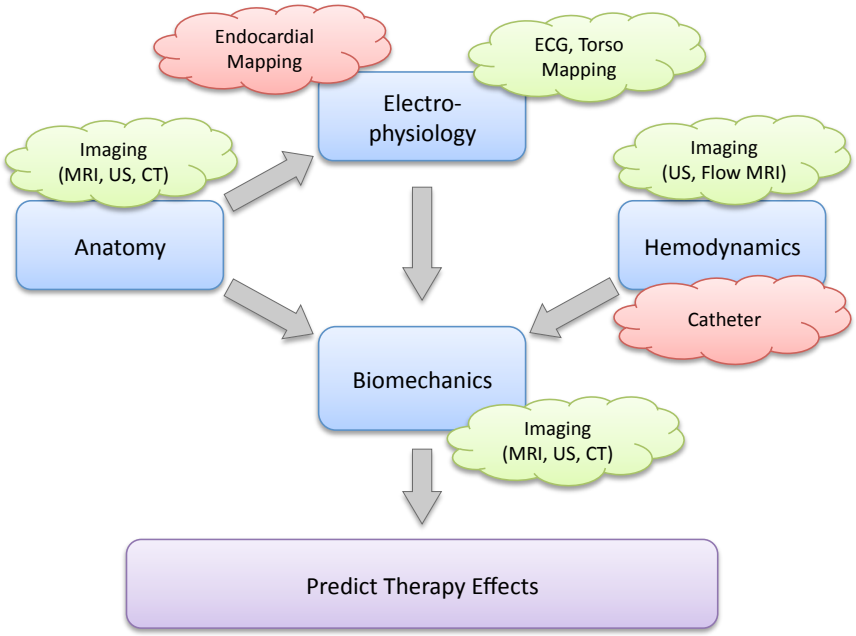


Figure 8. Framework for the personalised simulation of cardiac electromechanics. Each element is personalised from clinical data (non-invasive (*in green*) or invasive (*in red*)).

was semi-automatically segmented from short-axis cMRI and the myocardium mesh at mid-diastole was used as 3D anatomical model. The EM model, previously adapted to the specificities of rToF, was then personalised from the available clinical data (Sec. 4.1.). Afterwards, the EM model was employed to simulate PVR (Sec. 4.2.). Preoperative pulmonary regurgitation was disabled and virtual RV volume reduction was performed on the anatomical model using SOFA[1], an open source real-time soft-tissue intervention platform. Tested on two young patients, the model showed an improvement of both RV and LV function just after surgery (Sec. 4.3.)

4.1. Personalised Model of Cardiac Electromechanics in rToF

An EM model of the heart comprises four elements (Fig. 8): *i)* the anatomy, namely the cardiac geometry and its constituents; *ii)* electrophysiology, i.e. the electrical wave that triggers the cardiac motion; *iii)* biomechanics, i.e. the cardiac motion; and *iv)* hemodynamics, implemented in our model as boundary conditions. The following sections briefly outline each of these components. The reader is referred to [49, 86, 89] for further details.

4.1.1. Cardiac Anatomy Model

The cardiac anatomy model represents the geometry of the bi-ventricular myocardium and the orientation of the myocardium fibres.

[1] www.sofa-framework.org

Myocardium geometry is obtained from the mid-diastole time frame of a cMRI sequence (Fig. 9, top left panel). Any segmentation method can be used, from fully automatic [26, 31, 110] to more interactive approaches [48, 100]. A dynamic segmentation is obtained by propagating the mesh over the cardiac sequence [51, 105, 111]. From the myocardium surface at mid-diastole, we compute a tetrahedral mesh automatically (Fig. 9, top right panel) and label it for regional model calibration (Fig. 9, bottom left panel).

Nowadays, myocardium fibres cannot be imaged *in-vivo* in patients. Nevertheless, histological observations [8, 81, 95] and post-mortem diffusion tensor imaging [68, 70] suggested that fibre orientation is relatively constant. Their orientation with respect to the short axis plane varies from -70° on the epicardium to 0° at mid-wall to $+70^\circ$ on the endocardium. We thus generate synthetic fibres fitted to the patient myocardium geometry by linearly interpolating their orientation from -90° on the epicardium to 0° at mid-wall to $+90^\circ$ on the endocardium. Angles are slightly over-estimated to account for averaging, one fibre orientation being associated to one tetrahedron (Fig. 9, bottom right panel).

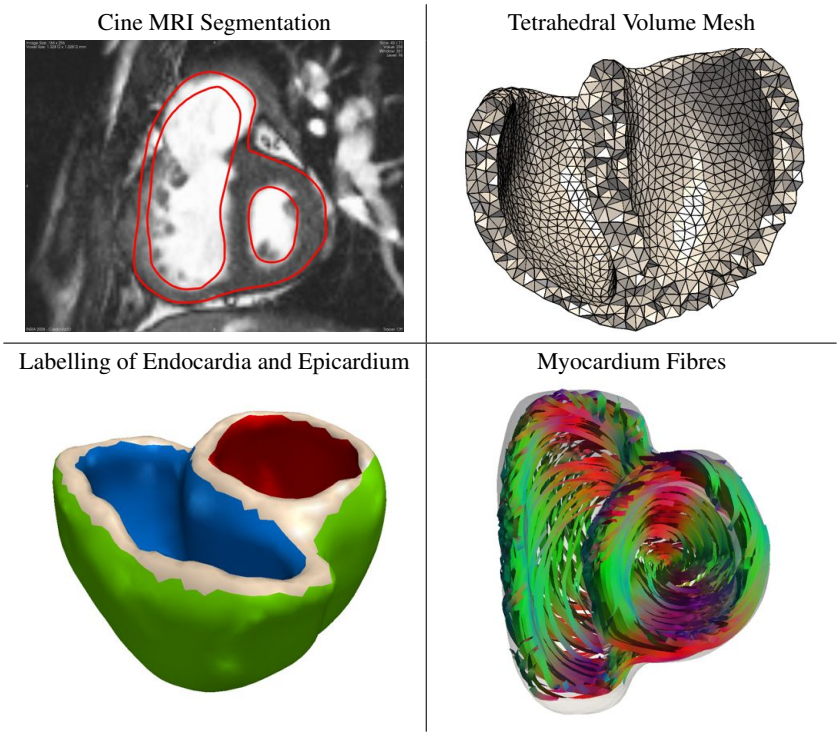


Figure 9. Personalised cardiac anatomy

4.1.2. Cardiac Electrophysiology Model

Next, we simulate the propagation of the electrical wave, namely the action potential, that triggers the cardiac contraction. Several electrophysiology models are available (see the review by Clayton and Panfilov [19] for instance). *Biophysical models* simulate in details the ionic interactions at the cell interfaces [65, 96]. They are controlled by more than fifty parameters related to the ionic interactions, parameters that are difficult to estimate from

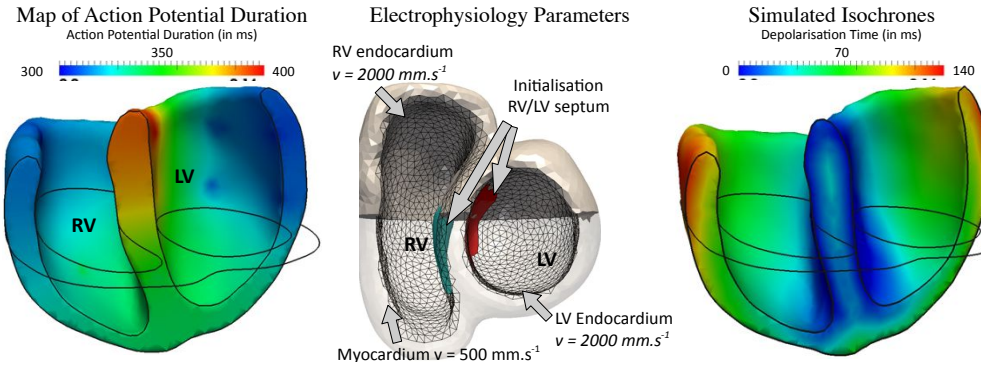


Figure 10. *Left panel*: Nominal action potential duration (APD). *Mid panel*: Main parameters of the cardiac electrophysiology model. *Right panel*: Simulated isochrones (colours correspond to depolarisation times). The electrical wave is initialised on the septal endocardia, then propagated over the endocardia and through the myocardium.

clinical data. *Phenomenological models* simulate the propagation of the electrical wave at a macroscopic scale [4, 30, 55, 60]. Simpler, they are controlled by two to three parameters. Methods to adjust these parameters from endocardial mapping for instance have been proposed recently [58, 74]. Finally, the *Eikonal models* only calculate the time when the electrical wave arrives at a given spatial position [21, 45]. They can be solved in almost real-time [67] thanks to the fast marching method [90]. They are controlled by one or two parameters, which can be adjusted from endocardial mapping for instance [17]. However, fibrillations and other complex pathologies cannot be simulated with Eikonal models.

The rToF patients we studied did not present severe electrophysiological abnormalities. We thus preferred the dynamic, anisotropic multi-front Eikonal model proposed in [87]. The depolarisation time T_d is computed at each vertex of the volume mesh according to the anisotropic Eikonal equation $v^2(\nabla T_d^t \, \mathrm{D} \, \nabla T_d) = 1$. In this equation, v is the local conduction velocity and D is the tensor relating to the conduction anisotropy, which writes in the coordinates along the fibre orientation $\mathbf{f}$, $\mathrm{D} = diag(1, \lambda, \lambda)$. λ is the conduction anisotropy ratio. It can be considered constant among individuals, $\lambda \in [0.3, 0.5]$ [19]. The repolarisation is controlled by the local action potential duration (APD) ($APD = 300\,ms$ at the free walls and $APD = 400\,ms$ at the septum [59], Fig. 10, left panel).

The bundle branches are modelled through large initialisation surface zones on the left and right septum (Fig. 10, mid panel). Each of these zones can be "excited" at different times to simulate bundle branch blocks. The conduction velocity v is about $500\,mm.s^{-1}$ within the myocardium and $v = 2000\,mm.s^{-1}$ on the endocardial surfaces to simulate the Purkinje fibres [59]. Fig. 10, right panel, illustrates some simulated isochrones with nominal electrophysiological parameters. Without biomechanics, electrophysiology simulation takes about 1 minute to compute.

4.1.3. Cardiac Biomechanics Model

The myocardium is an active, non-linear, anisotropic visco elastic tissue whose motion is triggered by the cardiac electrophysiology. Its constitutive law comprises an active element,

which models the active contraction of the muscle and is controlled by the action potential, and a passive element, which models the elasticity of the tissue.

A large variety of models have been proposed in the last decades to simulate the transient contractile force. The most detailed models simulate the ion interactions and the actin-myosin bindings that generate the cardiac motion [41,42,62,64]. They are controlled by a large number of parameters related to the ionic mechanisms, which makes them not readily suitable for personalised simulations. Multi-scale models have been proposed to cope with this limitation. They integrate biological mechanisms at different scale, yielding phenomenological equations at the organ level [10, 16, 79]. Resulting laws are controlled by fewer and clinically-meaningful parameters (usually 4 to 5 parameters).

Similarly, several models are available to simulate the passive properties of the myocardium. A first technique consists in using anisotropic linear elasticity [88], although that approach is accurate for small deformations only. Non-linear models are therefore preferred [69]. A standard approach is to derive the elastic stresses from non-linear stress-strain laws established *in-vitro* [22, 42]. Yet, improving the accuracy of the model is achieved at the price of complexity, with increasing number of parameters. The Costa law [22] for instance, which is often preferred as it models the anisotropy along the fibre direction and the fibre sheets, is governed by seven parameters, most of them difficult to estimate *in-vivo*.

Because we wanted to personalise the model from clinical data, we needed a fast but realistic biomechanical model. We thus relied on the model developed by Sermesant *et al.* [88], which simplifies the multi-scale phenomenological model proposed in [10]. Despite its relative simplicity, that model has been able to simulate the main features of the cardiac motion observed in images of healthy subjects and patients [85].

The equations of the model are solved using the finite element method (FEM) on linear tetrahedron. The passive properties are modelled by a linear anisotropic visco-elasticity model, controlled by the Young modulus E, which sets the elasticity of the tissue, and the Poisson ratio ν, which is used to ensure myocardium incompressibility ($\nu = 0.49$). The tissue is three times stiffer along the fibre direction [22]. The active contractile force along the fibre direction $\mathbf{f}$ is controlled by the depolarisation time T_d. For each vertex of the mesh, the contraction force $F_c = 1/4 \int_S \Sigma(t)\mathbf{n}dS$ is calculated. S is the surface of the tetrahedron, $\mathbf{n}$ the surface normal, and $\Sigma(t)$ is an anisotropic contraction tensor $\Sigma(t) = \sigma_c(t).\mathbf{f}\mathbf{f}^t$, $\sigma_c(t)$ being defined by:

$$\begin{cases} \text{if } T_d \leq t \leq T_d + APD: & \sigma_c(t) = \sigma_0 \left[1 - e^{\alpha_c (T_d - t)}\right] \\ \text{if } T_r < t < T_d + Heart\,Period: & \sigma_c(t) = \sigma_c(T_d + APD) e^{\alpha_r (T_d + APD - t)} \end{cases} \quad (1)$$

σ_0 is the maximum active contraction and α_c and α_r the contraction and relaxation rates respectively.

The cardiac motion is computed by solving the dynamic system $M\ddot{U} + C\dot{U} + KU = F_c + F_b$. In this equation, U is the displacement vector, $\dot{U}$ is the velocity of the nodes and $\ddot{U}$ their acceleration. M is the diagonal mass matrix calculated from the mass density of the myocardium $\rho = 1.07\,g/mL$, $C = d\dot{M}$ is a Rayleigh damping matrix ($d = 3000$) and K is the anisotropic linear elastic stiffness matrix based on the linear Hookean constitutive law. F_b captures the external boundary conditions (see next section). Model personalisation is achieved by adjusting, iteratively, σ_0, α_c, α_r and E.

4.1.4. Cardiac Hemodynamics Model and Boundary Conditions

Filling, isovolumetric contraction, ejection and isovolumetric relaxation are simulated as in [86]. During ejection (*resp.* filling), a pressure constraint equal to the arterial (*resp.* atrial) pressure is applied to the endocardia. Arterial pressures are simulated using a 3-element Windkessel model [94]. Blood flow across the valves is calculated as the variations of the blood pool volumes. During the isovolumetric phases, a penalty constraint is applied to the endocardia to keep the cavity volumes constant [11]. When the ventricular pressure becomes higher (*resp.* lower) than the arterial (*resp.* atrial) pressure, ejection (*resp.* filling) starts.

In this model of the cardiac phases, RV regurgitation affect the isovolumetric phases only, as the blood pool volume can now vary. Let Φ_c and Φ_r be the regurgitation flows at contraction and relaxation respectively. Φ_c and Φ_r can be estimated with echocardiography or phase-contrast MRI. The isovolumetric phases are modified such the variation of the blood pool volume matches the measured regurgitation flow. Let ΔV be the volume variation during Δt without isovolumetric constraint. If $|\Delta V| > |\Phi_{\{c,r\}}\Delta t|$, a penalty constraint is applied to each vertex of the RV endocardium such that the RV volume varies by $\Delta V = \Phi_{\{c,r\}}\Delta t$ exactly. Otherwise, no penalty constraint is applied.

Finally, the cardiac motion is prescribed into a 3D "pericardial" region. Inside that region, the heart is free to contract and twist, but it cannot go outside [48]. Weak springs are added to the myocardium base to simulate the effects of the atria and arteries on the longitudinal motion. As shown in [48], this approach yielded realistic cardiac motion, with downward basal displacements and relatively fixed apex.

4.2. Real-Time Simulation of Pulmonary Valve Replacement

Equipped with a virtual heart, we can now test the effects of PVR with RV volume reduction on the cardiac function of the patient. Replacing the valves amounts to stopping the regurgitation in the model. Surgical RV volume reduction is performed in SOFA, an open source soft-tissue intervention platform[2]. As illustrated in Fig. 11, the user interactively remodels the RV geometry by resecting regions of the RV free-wall (the RV aneurysm for instance). He then closes the free wall and sutures it to the septum to reconstruct the cavity. For the virtual surgery, the myocardium is modelled using linear elasticity corrected for large displacements and rotations of the elements using a with corotational FEM model [63]. Myocardium fibres are deformed consistently during the virtual surgery and the tetrahedra close to the surgical scar are labelled to simulate the effects of that scar on the postoperative cardiac function.

4.3. Experiment and Results

PVR with RV volume reduction was tested on two rToF patients who underwent comprehensive evaluation, echocardiography and magnetic resonance imaging (MRI). Retrospective SSFP cMRI of the heart were acquired in the short-axis view covering the entirety of both ventricles (1.5T scanner, Avanto, Siemens Medical Systems, Erlangen, Germany). To

[2] www.sofa-framework.org

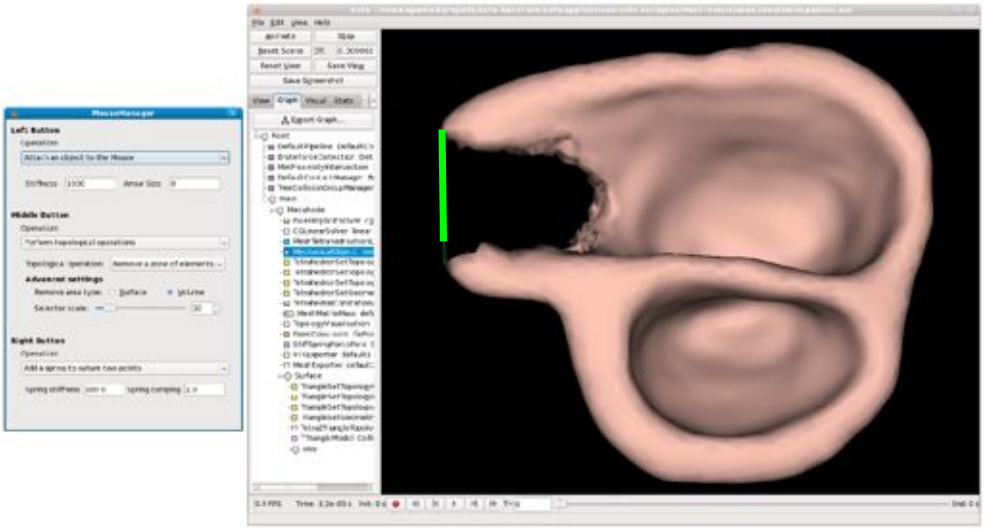


Figure 11. Virtual surgery. The anatomical model of a heart is being remodelled by the user. After resection, the free-wall is pulled close to the septum *(green line)*, before suturing. Cutting, closing and suturing interactions are performed in real-time.

date, none of these patients have undergone PVR. This means that no post-operative data were available to quantitatively validate the simulated postoperative cardiac function.

Patient 1: 16-year old boy recruited at Necker Enfants Malades, Hôpitaux de Paris, France. Echocardiography showed moderate pulmonary and tricuspid regurgitation with moderate RV dilation. RV pressure at end-systole was about $50\,mmHg$. Peak regurgitation flows Φ_c and Φ_r were estimated at $50\,mL.s^{-1}$. Visual inspection of the cMRI showed a dilated right ventricle outflow tract (RVOT). The RVOT was also dyskinetic, i.e. it dilated when the heart contracted. Nonetheless, LV and RV ejection fractions (EF), which quantify the pump efficiency of a chamber, were only slightly below normal. Electrophysiology was near normal.

Patient 2: 21-year old boy recruited at Great Ormond Street Hospital, London, U.K. Echocardiography showed moderate pulmonary regurgitation, mild tricuspid regurgitation and mild RV dilation. cMRI confirmed the mild RV dilation. A significant abnormal motion of the LV towards the RV was visible during systole. LV and RV EF were low. Electrophysiology was near normal.

4.3.1. Electromechanical Model Personalisation

Anatomy The compact bi-ventricular myocardium was interactively segmented from the end-diastole time frame of the cMRI sequence[3] [48, 100] and propagated along the cardiac sequence using the logDemons algorithm [102] (Sec. 2.). Blood pool volumes and EF were

[3] http://www-sop.inria.fr/asclepios/software/CardioViz3D/

calculated from the dynamic segmentation. Tetrahedral meshes were then computed from the segmentation at mid-diastole using CGAL [1] (patient 1: 59,768 elements; patient 2: 43,549 elements). LV, RV and any abnormal region visible on the cMRI were automatically mapped onto the meshes for regional adjustment. Finally, fibre orientations were generated from the patient geometry. The anatomical models of the two patients are illustrated in Fig. 12.

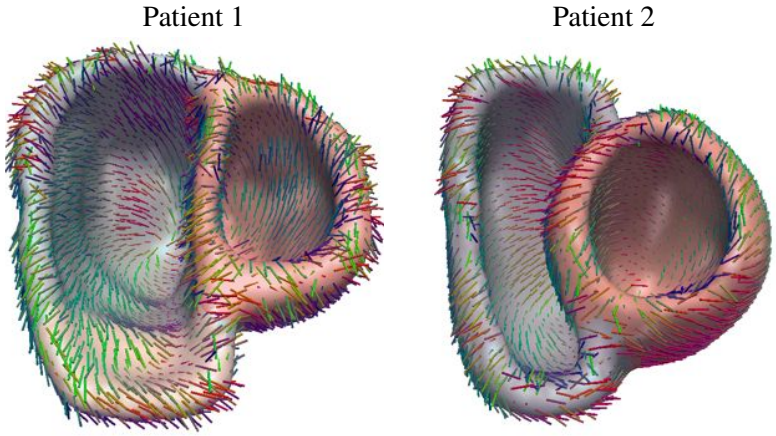


Figure 12. Personalised anatomical models. *In red*: LV. *In blue*: RV. *In brown*: dyskinetic area. *Colour lines*: Myocardium fibres.

Electrophysiology Both patients did not suffer from major electrophysiological troubles. We thus kept the electrophysiology parameters nominal. The simulations were synchronised with the cMRI motion using the beginning of systole.

Biomechanics Myocardium elasticity was kept nominal in both patients ($E = 50 MPa$ [92]). The maximum contraction σ_0 was adjusted such that the simulated heart reaches the true position at end-systole. The rates α_c and α_r were calibrated to reproduce the speed of contraction and relaxation respectively. The contractility of the dyskinetic regions was disabled to capture their abnormal motion. All these parameters were adjusted iteratively through trial and errors, which was possible as one heart beat took only 15 to 30 minutes to compute (MacPro 3.2GHz Quad-Core Intel Xeon, 16GB of RAM). Basically, the simulation for a given set of parameters was qualitatively compared with the cardiac motion visible on the cMRI. At the same time, the simulated variation of the blood pool volumes was quantitatively compared with the ground truth given by the dynamic segmentation. If the simulation did not match the true cardiac motion, the parameters were slightly modified accordingly and the simulation re-run, until convergence. Table 1 reports the final parameters for each patient. Two observations can be done at this stage. First, RV contractility was lower than normal, probably because of its dilated morphology and possible fibrosis due to the long term over-load. Second, the parameters were fairly similar between the two patients. This is very encouraging for future mainstream applications.

Hemodynamics The parameters of the arterial Windkessel model were set according to the literature [106]. Regurgitation flows Φ_c and Φ_r were measured using echocardiography (Table 1).

Table 1. Adjusted parameters of the cardiac model. Non-reported parameters were kept at their nominal values *(see text for details)*.

Parameters	Nominal	Patient 1	Patient 2
Maximum contraction σ_0 (in $kPa.mm^{-2}$)	$\sigma_0 = 100$	$\sigma_0 = 100$ $\sigma_{0_{RV}} = 70$ $\sigma_{0_{dysk}} = 0$	$\sigma_{0_{LV}} = 70$ $\sigma_{0_{RV}} = 70$
Contraction rate α_c (in s^{-1})	$\alpha_c = 10$	$\alpha_c = 10$	$\alpha_{c_{LV}} = 15$ $\alpha_{c_{RV}} = 5$
Relaxation rate α_r (in s^{-1})	$\alpha_r = -20$	$\alpha_r = -10$	$\alpha_r = -10$
RV regurgitation flows Φ_c, Φ_r (in $mL.s^{-1}$)	$\Phi_c = \Phi_r \simeq 0$	$\Phi_c = \Phi_r \simeq 50$	$\Phi_c = \Phi_r \simeq 30$

4.3.2. Preoperative Simulation

After model adjustment, realistic ejection fractions (Table 2) and volume variations (Fig. 13) were obtained. We recall that the ejection fraction is computed from the blood pool volumes at end diastole EDV and at end systole ESV by $EF = (EDV - ESV)/EDV$. The EM model managed to provide, for these patients, realistic contraction patterns. Simulated radial displacements computed from the mid-diastole position were locally consistent with those computed from the segmentation. In particular, the dyskinetic RVOT observed in the first patient was fairly captured by the model (Fig. 14). The abnormal leftwards motion of the heart of the second patient was also satisfyingly recovered (Fig. 15). The estimated model parameters suggested that this abnormal motion resulted from the RV weak contractility and dilation.

Capturing cardiac relaxation was more difficult, in particular for the second patient. That limitation may be due to the generic electrical activation pattern (no clinical data was available to finely calibrate the electrophysiology) or the lack of explicit model of early myocardial relaxation [84].

Finally, although fairly simple, our regurgitation model yielded pressure-volume loops consistent with measurements in rToF reported in the literature [73]. Unfortunately, these data were not available for comparisons.

4.3.3. Simulation of PVR with RV Volume Reduction

We then simulated PVR with RV volume reduction on the personalised cardiac models as described in Sec. 4.2. (Fig. 16). The dyskinetic regions were removed and the RV volume reduced interactively. The postoperative scar was simulated by disabling the electrical conductivity ($v = 0 m.s^{-1}$) and the active contractility ($\sigma_0 = 0 MPa$) locally.

Table 2. Ejection fractions (EF) in percentage. The personalised EM model managed to capture patients EF. PVR with RV volume reduction improved both RV and LV EF, suggesting a tight relationship between RV and LV functions.

	Patient 1		**Patient 2**	
	$LVEF$	$RVEF$	$LVEF$	$RVEF$
Segmentation	61%	41%	42%	40%
Simulation: Preoperative	59%	40%	41%	37%
Simulation: PVR with RV reduction	63%	51%	54%	46%

After PVR, RV volume decreased as a consequence of the surgery (Fig. 13, red curve) and RV postoperative EF improved significantly (Table 13). Interestingly, the simulated LV function also improved in both patients, although we did not modified its anatomy nor its electromechanical parameters. This experiment highlights a tight relationship between the two cavities through the inter-ventricular septum.

4.4. Discussion

Image processing techniques, electromechanical models and virtual soft-tissue intervention platforms open the premises to *in-silico* planning of PVR on rToF patients. The lack of postoperative data prevented us from validating the simulated PVR effects and, as a consequence, our cardiac model. Yet, obtained results were found qualitatively reasonable by cardiologists, which encourages further work in that direction.

Although simplified, the model was able to capture the cardiac function of the patients. Lesion removal and direct RV volume reduction improved the bi-ventricular function by improving the RV contraction and minimising abnormal septal motion. Cardiac modelling and virtual surgery could thus assist the surgeon in planing the operation that optimises the postoperative outcome. Nonetheless, this procedure is invasive (open-heart surgery) and risky for the patient. Moreover, the long term outcome is not clear as this approach is relatively recent [23]. In particular, subsequent heart remodelling may reduce the positive effects of the surgical RV volume reduction to accommodate the surgical scar. It could therefore be interesting to model the postoperative cardiac remodelling. A possible direction would consist in using the statistical models presented in Sec. 3. for instance.

Several research directions can be explored to improve the proposed framework. First, the approach must be validated *a posteriori*, on postoperative data or with animal experiments. This is a mandatory step before bringing these tools into the clinics. It has to be noted however that similar experiments on adults with heart failure showed promising predictive powers of the model [85]. Second, the regurgitation model can be improved to better take into account the fluid dynamics. Fluid-structure interactions and computational fluid dynamics could be coupled with our finite element electromechanical model for instance [33, 54, 107]. Third, the biomechanical model should be enhanced with more realistic non-linear laws [22] and more detailed electromechanical coupling [10] that can simulate the early active relaxation. Finally, the whole approach would greatly benefit from automated parameter estimation methods [11, 17, 74]. More patients could be processed. In parallel, identified parameters would be used as quantitative features of the cardiac condi-

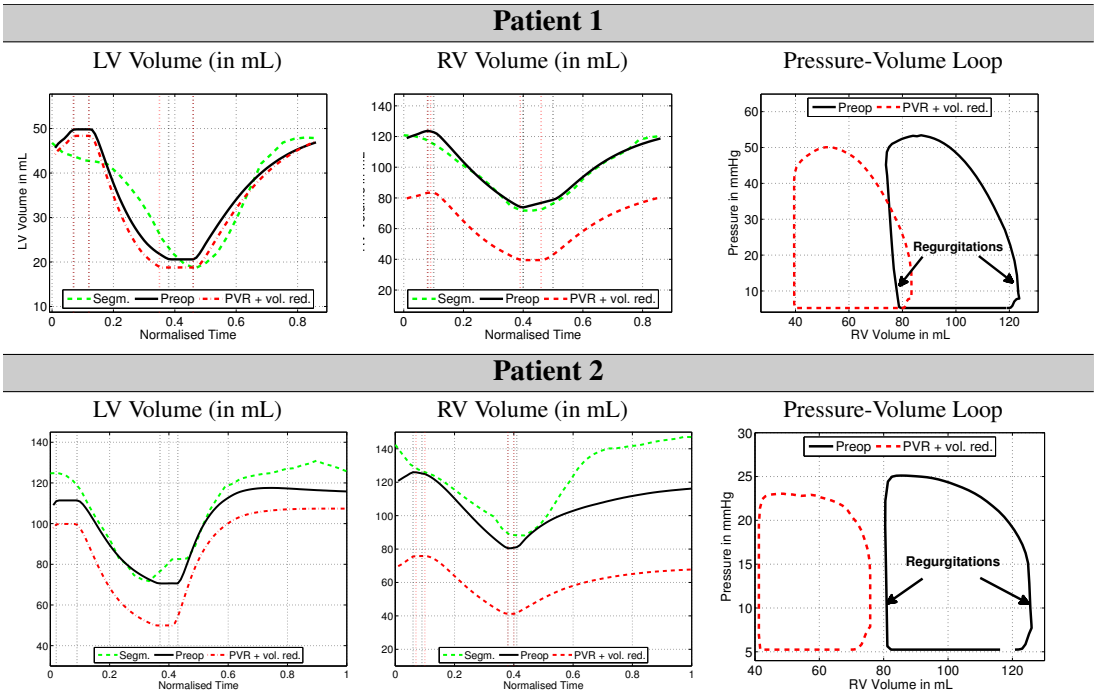


Figure 13. RV volume curves and pressure-volume loops. Volume curves are computed from segmentation *(green curves)* and simulations *(black, blue and red curves)*. Vertical bars delineate the simulated cardiac phases. Regurgitations are visible in the pressure volume loops. During the isovolumetric phases, volume changes instead of being constant. *(See text for details)*

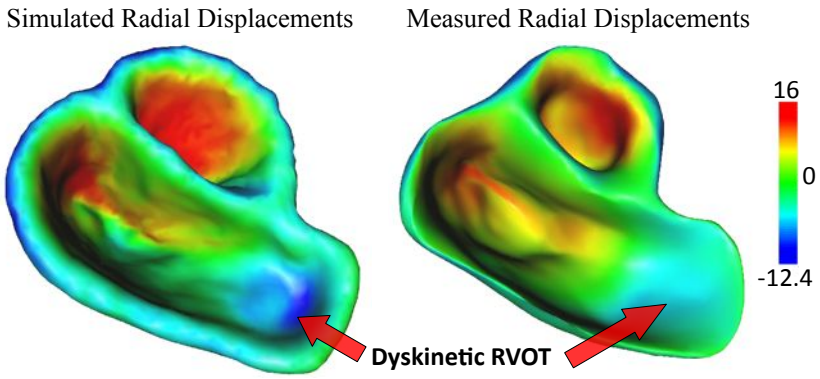


Figure 14. Radial displacements (in mm) at end-systole of the first patient, computed with respect to the end-diastole position. Positive values denote inward motion. As suggested by the similar colour patterns between simulation and segmentation, the EM model was able to exhibit realistic motion, in particular the dyskinetic right ventricle outflow tract (RVOT).

tion for diagnostic support.

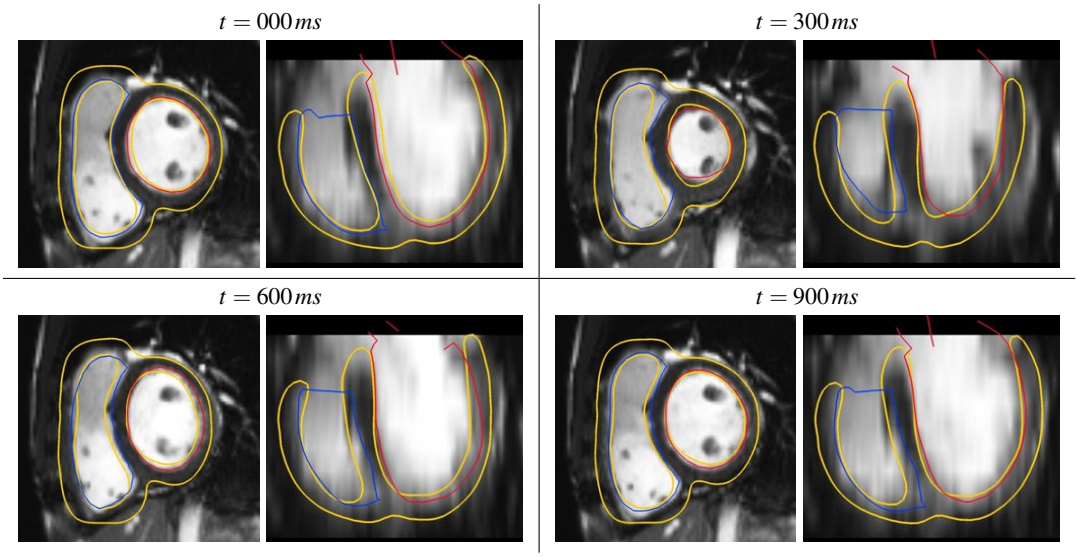


Figure 15. Personalised simulation of the second patient (*yellow*) overlaid on the cMRI. Segmentation contours are in red (LV) and blue (RV). Although not guided by the images, the model managed to capture the abnormal leftward translation of the LV due to the dilated and impaired RV.

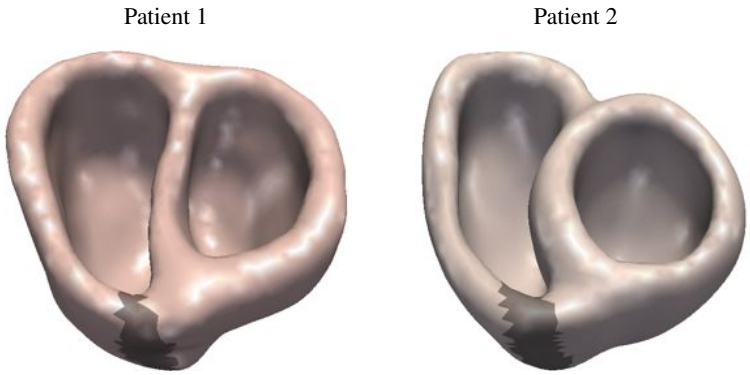


Figure 16. Postoperative anatomies. Surgical scar in black.

5. Conclusion

In this chapter we presented three image-driven models of the heart for diagnosis, prognosis and therapy planning in repaired tetralogy of Fallot. The promising results obtained so far encourage future work in that direction. Nowadays, it is acknowledged that computational models of the heart will have a tremendous impact on the clinical workflow, and more especially in congenital heart diseases. In the long term, electromechanical models would be used as integrative tools. They will integrate knowledge from images, signals and clinical reports into a common framework, synthesising all this information to reproduce the cardiac function of the patient in the computer. The cardiologist will then be able to test different therapeutical strategies *in-silico* and decide the most appropriate therapy for a

specific patient.

Yet, much remains to be done to reach that goal. Several difficulties remain to be solved. The most important question to tackle is the adequacy of the model with the clinical data. A compromise between model accuracy and parameter observability must be found, by focussing on a specific clinical questions for instance. The quality of the available data is also an important factor to consider, leading the researcher to choose one model rather than another because its parameters cannot be estimated from the available data. In parallel, efficient inverse problems method must be developed to estimate the parameters of the models automatically. Finally, a thorough effort of validation is mandatory before applying these methods in the clinical routine. Despite these difficulties, the encouraging results presented in that chapter and those that appeared recently in the literature pushes the community to strive hard towards that direction.

Acknowledgement These works were partially funded by the European integrated project Health-e-Child (IST-2004-027749). The authors warmly thank the cardiologists involved in these studies, in particular Younes Boudjemline, Necker Enfants Malades, APHP, Paris, France; Andrew Taylor, Great Ormond Street Hospital, London, U.K.; Benedetta Leonardi and Giacomo Pongiglione, Ospedale Pediatrico Bambino Gesù, Rome, Italy. We also thank Erik Pernod, for his help to set up the virtual surgery platform and Ingmar Voigt, Medical Informatics, Siemens Corporate Research, Princeton, NJ, USA and Pattern Recognition Lab, University of Erlangen-Nuremberg, for the segmentations of the right ventricle.

References

[1] CGAL, Computational Geometry Algorithms Library. http://www.cgal.org.

[2] C. Alberto Figueroa, S. Baek, C. Taylor, and J. Humphrey. A computational framework for fluid-solid-growth modeling in cardiovascular simulations. *Computer methods in applied mechanics and engineering*, 198(45-46):3583–3602, 2009.

[3] A. Aletras, S. Ding, R. Balaban, and H. Wen. Dense: displacement encoding with stimulated echoes in cardiac functional mri. *Journal of Magnetic Resonance*, 137(1):247–252, 1999.

[4] R. R. Aliev and A. V. Panfilov. A simple two-variable model of cardiac excitation. *Chaos, Solitons & Fractals*, 7(3):293–301, March 1996.

[5] J. Allard, S. Cotin, F. Faure, P.-J. Bensoussan, F. Poyer, C. Duriez, H. Delingette, and L. Grisoni. SOFA – an Open Source Framework for Medical Simulation. In *Medicine Meets Virtual Reality (MMVR'15)*, 2007.

[6] S. Allassonniere, Y. Amit, and A. Trouve. Towards a coherent statistical framework for dense deformable template estimation. *Journal of the Royal Statistical Society: Series B (Statistical Methodology)*, 69(1):3–29, 2007.

[7] V. Arsigny, O. Commowick, X. Pennec, and N. Ayache. A log-euclidean framework for statistics on diffeomorphisms. In *Medical Image Computing and Computer Assisted Intervention (MICCAI)*, volume 4190 of *Lecture Notes in Computer Science*, page 924. Springer, 2006.

[8] T. Arts, K. D. Costa, J. W. Covell, and A. D. McCulloch. Relating myocardial laminar architecture to shear strain and muscle fiber orientation. *Am J Physiol Heart Circ Physiol*, 280(5):H2222–2229, 2001.

[9] K. Arun, T. Huang, and S. Blostein. Least-squares fitting of two 3-D point sets. *IEEE Transactions on Pattern Analysis and Machine Intelligence*, 9(5):698–700, September 1987.

[10] J. Bestel, F. Clement, and M. Sorine. A biomechanical model of muscle contraction. In *Medical Image Computing and Computer Assisted Intervention (MICCAI)*, Lecture Notes in Computer Science, pages 1159–1161. Springer, 2001.

[11] F. Billet. *Assimilation de données images pour la personnalisation d'un modèle électromécanique du cœur*. PhD thesis, Université de Nice-Sophia Antipolis, 2010.

[12] A. Bistoquet, J. Oshinski, and O. Skrinjar. Myocardial deformation recovery from cine MRI using a nearly incompressible biventricular model. *Medical Image Analysis*, 12(1):69–85, 2008.

[13] N. Bodhey, P. Beerbaum, S. Sarikouch, S. Kropf, P. Lange, F. Berger, R. Anderson, and T. Kuehne. Functional Analysis of the Components of the Right Ventricle in the Setting of Tetralogy of Fallot. *Circulation: Cardiovascular Imaging*, 1(2):141, 2008.

[14] C. Broit. *Optimal registration of deformed images*. PhD thesis, University of Pennsylvania Philadelphia, PA, USA, 1981.

[15] P. Cachier and N. Ayache. Isotropic energies, filters and splines for vectorial regularization. *J. of Math. Imaging and Vision*, 20(3):251–265, 2004.

[16] D. Caillerie, A. Mourad, and A. Raoult. Cell-to-muscle homogenization. application to a constitutive law for the myocardium. *Mathematical Modelling and Numerical Analysis*, 37(4):681–698, 2003.

[17] P. Chinchapatnam, K. Rhode, M. Ginks, C. Rinaldi, P. Lambiase, R. Razavi, S. Arridge, and M. Sermesant. Model-based imaging of cardiac apparent conductivity and local conduction velocity for diagnosis and planning of therapy. *IEEE Transactions on Medical Imaging*, 27(11):1631–1642, 2008.

[18] E. Chung, A. Leon, L. Tavazzi, J. Sun, P. Nihoyannopoulos, J. Merlino, W. Abraham, S. Ghio, C. Leclercq, J. Bax, et al. Results of the predictors of response to crt (prospect) trial. *Circulation*, 117(20):2608, 2008.

[19] R. Clayton and A. Panfilov. A guide to modelling cardiac electrical activity in anatomically detailed ventricles. *Progress in biophysics and molecular biology*, 96(1-3):19–43, 2008.

[20] A. Cobanoglu and J. Schultz. Total correction of tetralogy of Fallot in the first year of life: late results. *The Annals of thoracic surgery*, 74(1):133–138, 2002.

[21] P. Colli Franzone, L. Guerri, and S. Rovida. Wavefront propagation in an activation model of the anisotropic cardiac tissue: asymptotic analysis and numerical simulations. *Journal of mathematical biology*, 28(2):121–176, 1990.

[22] K. Costa, J. Holmes, and D. McCulloch. Modelling cardiac mechanical properties in three dimensions. *Philosophical Transactions A*, 359(1783):1233, 2001.

[23] P. del Nido. Surgical management of right ventricular dysfunction late after repair of tetralogy of fallot: right ventricular remodeling surgery. In *Seminars in Thoracic and Cardiovascular Surgery: Pediatric Cardiac Surgery Annual*, volume 9, pages 29–34. Elsevier, 2006.

[24] B. Delhay, P. Clarysse, and I. Magnin. Locally Adapted Spatio-temporal Deformation Model for Dense Motion Estimation in Periodic Cardiac Image Sequences. In *FIMH*, volume 4466, page 393. Springer, 2007.

[25] S. Durrleman, X. Pennec, A. Trouvé, and N. Ayache. Statistical models on sets of curves and surfaces based on currents. *Medical Image Analysis*, 13(5):793–808, Oct. 2009.

[26] O. Ecabert, J. Peters, H. Schramm, C. Lorenz, J. von Berg, M. J. Walker, M. Vembar, M. E. Olszewski, K. Subramanyan, G. Lavi, and J. Weese. Automatic model-based segmentation of the heart in ct images. *IEEE Transactions on Medical Imaging*, 27(9):1189–1201, 2008.

[27] L. C. Evans. *Partial Differential Equations*. American Mathematical Society, June 1998.

[28] L. Feng, R. Donnino, J. Babb, L. Axel, and D. Kim. Numerical and in vivo validation of fast cine displacement-encoded with stimulated echoes (dense) mri for quantification of regional cardiac function. *Magnetic Resonance in Medicine*, 62(3):682–690, 2009.

[29] W. Feng, T. Denney, S. Lloyd, L. Dell'Italia, and H. Gupta. Contour regularized left ventricular strain analysis from cine MRI. In *Biomedical Imaging: From Nano to Macro, 2008. ISBI 2008. 5th IEEE International Symposium on*, pages 520–523, 2008.

[30] R. Fitzhugh. Impulses and physiological states in theoretical models of nerve membrane. *Biophysical Journal*, 1(6):445–466, 1961.

[31] A. Frangi, W. Niessen, and M. Viergever. Three-dimensional modeling for functional analysis of cardiac images: A review. *IEEE Transactions on Medical Imaging*, 20(1):2–5, 2001.

[32] A. Frigiola, V. Tsang, J. Nordmeyer, P. Lurz, C. van Doorn, A. Taylor, P. Bonhoeffer, and M. de Leval. Current approaches to pulmonary regurgitation. *European Journal of Cardio-Thoracic Surgery*, 34(3):576, 2008.

[33] J. Gerbeau, M. Vidrascu, and P. Frey. Fluid-structure interaction in blood flows on geometries based on medical imaging. *Computers & Structures*, 83(2-3):155–165, 2005.

[34] T. Geva. Indications and timing of pulmonary valve replacement after tetralogy of Fallot repair. In *Seminars in Thoracic and Cardiovascular Surgery: Pediatric Cardiac Surgery Annual*, volume 9, pages 11–22. Elsevier, 2006.

[35] L. Glass, P. Hunter, and A. McCulloch. *Theory of Heart: Biomechanics, Biophysics, and Nonlinear Dynamics of Cardiac Function*. Springer-Verlag, 1991.

[36] J. Glaunes. *Modeles déformables en appariement de formes. Transport par difféomorphismes de points, de mesures et de courants pour la comparaison de formes et l'anatomie numérique*. PhD thesis, Phd Thesis (in french), Université Paris 13, 2005.

[37] A. Guimond, J. Meunier, and J.-P. Thirion. Average brain models: A convergence study. *Computer Vision and Image Understanding*, 77(2):192–210, 2000.

[38] E. Haber and J. Modersitzki. Numerical methods for volume preserving image registration. *Inverse Problems*, 20(5):1621–1638, 2004.

[39] J. Hamm, D. Ye, R. Verma, and C. Davatzikos. Gram: A framework for geodesic registration on anatomical manifolds. *Medical Image Analysis*, 2010.

[40] P. Hunter, T. Borg, and P. Box. Integration from proteins to organs: the physiome project. *Nature Reviews Molecular Cell Biology*, 4:237–243, 2003.

[41] P. Hunter, A. McCulloch, and H. Ter Keurs. Modelling the mechanical properties of cardiac muscle. *Progress in biophysics and molecular biology*, 69(2-3):289–331, 1998.

[42] P. Hunter and B. Smaill. The analysis of cardiac function: a continuum approach. *Prog Biophys Mol Biol*, 52(2):101–164, 1988.

[43] P. J. Hunter, A. J. Pullan, and B. H. Smaill. Modeling total heart function. *Annu Rev Biomed Eng*, 5:147–177, 2003.

[44] S. Joshi, B. Davis, M. Jomier, and G. Gerig. Unbiased diffeomorphic atlas construction for computational anatomy. *NeuroImage*, 23:151–160, 2004.

[45] J. Keener and J. Sneyd. *Mathematical physiology*. Springer-Verlag, 1998.

[46] S. Khambadkone, L. Coats, A. Taylor, Y. Boudjemline, G. Derrick, V. Tsang, J. Cooper, V. Muthurangu, S. R. Hegde, R. S. Razavi, D. Pellerin, J. Deanfield, and P. Bonhoeffer. Percutaneous pulmonary valve implantation in humans: Results in 59 consecutive patients. *Circulation*, 112(8):1189–1197, 2005.

[47] W. Kroon, T. Delhaas, T. Arts, and P. Bovendeerd. Constitutive modeling of cardiac tissue growth. In *Functional Imaging and Modeling of the Heart*, volume 4466 of *Lecture Notes in Computer Science*, page 340. Springer, 2007.

[48] T. Mansi. *Image-Based Physiological and Statistical Models of the Heart, Application to Tetralogy of Fallot*. Thèse de sciences (PhD thesis), Ecole Nationale Supérieure des Mines de Paris, September 2010.

[49] T. Mansi, B. André, M. Lynch, M. Sermesant, H. Delingette, Y. Boudjemline, and N. Ayache. Virtual pulmonary valve replacement interventions with a personalised cardiac electromechanical model. In *Recent Advances in the 3D Physiological Human*, volume 5528 of *Lecture Notes in Computer Science*, pages 201–210. Springer, 2009.

[50] T. Mansi, S. Durrleman, B. Bernhardt, M. Sermesant, H. Delingette, I. Voigt, P. Lurz, A. M. Taylor, J. Blanc, Y. Boudjemline, X. Pennec, and N. Ayache. A Statistical Model of Right Ventricle in Tetralogy of Fallot for Prediction of Remodelling and Therapy Planning. In *Medical Image Computing and Computer Assisted Intervention (MICCAI)*, volume 5761 of *Lecture Notes in Computer Science*, pages 214–221, London, UK, Sept. 2009. Springer.

[51] T. Mansi, X. Pennec, M. Sermesant, H. Delingette, and N. Ayache. iLogDemons: A Demons-Based Registration Algorithm for Tracking Incompressible Elastic Biological Tissues. *Int. J. of Computer Vision*, 2010. To appear.

[52] A. McCulloch, J. Bassingthwaighte, P. Hunter, and D. Noble. Computational biology of the heart: from structure to function. *Prog Biophys Mol Biol*, 69(2-3), 1998.

[53] E. McVeigh. Regional myocardial function. *Cardiology Clinics*, 16(2):189–206, 1998.

[54] V. Mihalef, D. Metaxas, M. Sussman, V. Hurmusiadis, and L. Axel. Atrioventricular blood flow simulation based on patient-specific data. In *Functional Imaging and Modeling of the Heart*, Lecture Notes in Computer Science, pages 386–395. Springer, 2009.

[55] C. Mitchell and D. Schaeffer. A two-current model for the dynamics of cardiac membrane. *Bulletin of mathematical biology*, 65(5):767–793, 2003.

[56] J. Modersitzki. *Numerical Methods for Image Registration*. Oxford University Press, 2004.

[57] C. Moore, C. Lugo-Olivieri, E. McVeigh, and E. Zerhouni. Three-dimensional systolic strain patterns in the normal human left ventricle: Characterization with tagged MR imaging. *Radiology*, 214(2):453–466, 2000.

[58] V. Moreau-Villéger, H. Delingette, M. Sermesant, H. Ashikaga, E. McVeigh, and N. Ayache. Building maps of local apparent conductivity of the epicardium with a 2d electrophysiological model of the heart. *IEEE Transactions on Biomedical Engineering*, 53(8):1457–1466, August 2006.

[59] F. Murgatroyd and A. Krahn. *Handbook of cardiac electrophysiology: A practical guide to invasive EP studies and catheter Ablation*. Remedica, 2002.

[60] J. Nagumo, S. Arimoto, and S. Yoshizawa. An active pulse transmission line simulating nerve axon. *Proceedings of the IRE*, 50(10):2061–2070, 1962.

[61] M. Nash. *Mechanics and material properties of the heart using an anatomically accurate mathematical model*. PhD thesis, University of Auckland, 1998.

[62] M. Nash and P. Hunter. Computational mechanics of the heart. *Journal of elasticity*, 61(1):113–141, 2000.

[63] M. Nesme, Y. Payan, and F. Faure. Efficient, physically plausible finite elements. *Eurographics (short papers)*, pages 77–80, 2005.

[64] S. Niederer and N. Smith. An improved numerical method for strong coupling of excitation and contraction models in the heart. *Progress in biophysics and molecular biology*, 96(1-3):90–111, 2008.

[65] D. Noble. A modification of the hodgkin—huxley equations applicable to purkinje fibre action and pacemaker potentials. *The Journal of Physiology*, 160(2):317, 1962.

[66] X. Papademetris, A. Sinusas, D. Dione, R. Constable, and J. Duncan. Estimating 3D strain from 4D cine-MRI and echocardiography: In-vivo validation. In *Medical Image Computing and Computer Assisted Intervention (MICCAI)*, Lecture Notes in Computer Science, pages 678–686. Springer, 2000.

[67] E. Pernod, M. Sermesant, J. Relan, and H. Delingette. Interactive real time simulation of cardiac radio-frequency ablation. In *Proc. of Eurographics Workshop on Visual Computing for Biology and Medicine (2010) (VCBM'2010)*, Leipzig, August 2010.

[68] J.-M. Peyrat, M. Sermesant, X. Pennec, H. Delingette, C. Xu, E. R. McVeigh, and N. Ayache. A computational framework for the statistical analysis of cardiac diffusion tensors: Application to a small database of canine hearts. *IEEE TMI*, 26(11):1500–1514, 2007.

[69] G. Picinbono, H. Delingette, and N. Ayache. Non-linear anisotropic elasticity for real-time surgery simulation. *Graphical Models*, 65(5):305–321, September 2003.

[70] M. Pop, M. Sermesant, T. Mansi, E. Crystal, J. Detsky, Y. Yang, P. Fefer, E. McVeigh, A. Dick, and N. Ayache. Characterization of post-infarct scars in a porcine model–a combined experimental and theoretical study. In *Proceedings of the 5th International Conference on Functional Imaging and Modeling of the Heart*, page 10. Springer, 2009.

[71] A. Qiu, L. Younes, M. Miller, and J. Csernansky. Parallel transport in diffeomorphisms distinguishes the time-dependent pattern of hippocampal surface deformation due to healthy aging and the dementia of the alzheimer's type. *NeuroImage*, 40(1):68–76, 2008.

[72] A. Rao, G. Sanchez-Ortiz, R. Chandrashekara, M. Lorenzo-Valdes, R. Mohiaddin, and D. Rueckert. Comparison of cardiac motion across subjects using non-rigid registration. In *Medical Image Computing and Computer Assisted Intervention (MICCAI)*, Lecture Notes in Computer Science, pages 722–729. Springer, 2002.

[73] A. N. Redington, M. L. Rigby, E. A. Shinebourne, and P. J. Oldershaw. Changes in the pressure-volume relation of the right ventricle when its loading conditions are modified. *Br. Heart J.*, 63(1):45–49, 1990.

[74] J. Relan, P. Chinchapatnam, H. Delingette, K. Rhode, R. Razavi, N. Ayache, , and M. Sermesant. Coupled personalisation of electrophysiology models for simulation of induced ischemic ventricular tachycardia. In *Medical Image Computing and Computer Assisted Intervention (MICCAI)*, LNCS. Springer, 2010. To appear.

[75] E. Rodriguez, A. Hoger, and A. McCulloch. Stress-dependent finite growth in soft elastic tissues. *Journal of biomechanics*, 27(4):455–467, 1994.

[76] T. Rohlfing, C. Maurer Jr, D. Bluemke, and M. Jacobs. Volume-preserving nonrigid registration of MR breast images using free-form deformation with an incompressibility constraint. *IEEE Transactions on Medical Imaging*, 22(6):730–741, 2003.

[77] R. Rosipal and N. Krämer. Overview and recent advances in partial least squares. *Subspace, Latent Structure and Feature Selection*, pages 34–51, 2006.

[78] K. A. Saddi, C. Chefd'hotel, and F. Cheriet. Large deformation registration of contrast-enhanced images with volume-preserving constraint. In *Proceedings of SPIE Medical Imaging*, volume 6512. SPIE, 2007.

[79] J. Sainte-Marie, D. Chapelle, R. Cimrman, and M. Sorine. Modeling and estimation of the cardiac electromechanical activity. *Computers & Structures*, 84(28):1743–1759, 2006.

[80] M. Samyn, A. Powell, R. Garg, L. Sena, and T. Geva. Range of ventricular dimensions and function by steady-state free precession cine MRI in repaired tetralogy of Fallot: right ventricular outflow tract patch vs. conduit repair. *Journal of Magnetic Resonance Imaging*, 26(4):934–940, 2007.

[81] D. Sanchez-Quintana, R. Anderson, and S. Ho. Ventricular myoarchitecture in tetralogy of fallot. *British Medical Journal*, 76(3):280, 1996.

[82] J. Schaerer, C. Casta, J. Pousin, and P. Clarysse. A dynamic elastic model for segmentation and tracking of the heart in mr image sequences. *Medical Image Analysis*, 2010.

[83] R. Scherptong, M. Hazekamp, B. Mulder, O. Wijers, C. Swenne, E. van der Wall, M. Schalij, and H. Vliegen. Follow-Up After Pulmonary Valve Replacement in Adults With Tetralogy of Fallot:: Association Between QRS Duration and Outcome. *Journal of the American College of Cardiology*, 56(18):1486–1492, 2010.

[84] P. Sengupta, B. Khandheria, and J. Narula. Twist and untwist mechanics of the left ventricle. *Heart Failure Clinics*, 4(3):315–324, 2008.

[85] M. Sermesant, F. Billet, R. Chabiniok, T. Mansi, P. Chinchapatnam, P. Moireau, J.-M. Peyrat, K. Rhode, M. Ginks, P. Lambiase, S. Arridge, H. Delingette, M. Sorine, A. Rinaldi, D. Chapelle, R. Razavi, and N. Ayache. Personalised electromechanical model of the heart for the prediction of the acute effects of cardiac resynchronisation therapy. In *Proceedings of Functional Imaging and Modeling of the Heart 2009 (FIMH'09)*, volume 5528 of *Lecture Notes in Computer Science*, pages 239–248, 3-5 June 2009.

[86] M. Sermesant, H. Delingette, and N. Ayache. An electromechanical model of the heart for image analysis and simulation. *IEEE TMI*, 25(5):612–625, 2006.

[87] M. Sermesant, E. Konukoglu, H. Delingette, Y. Coudiere, P. Chinchapatnam, K. Rhode, R. Razavi, and N. Ayache. An anisotropic multi-front fast marching method for real-time simulation of cardiac electrophysiology. *Proc. FIMH 2007*, 9:160–169, 2007.

[88] M. Sermesant, P. Moireau, O. Camara, J. Sainte-Marie, R. Andriantsimiavona, R. Cimrman, D. L. Hill, D. Chapelle, and R. Razavi. Cardiac function estimation from MRI using a heart model and data assimilation: Advances and difficulties. *Medical Image Analysis*, 10(4):642–656, 2006.

[89] M. Sermesant, J. Peyrat, P. Chinchapatnam, F. Billet, T. Mansi, K. Rhode, H. Delingette, R. Razavi, and N. Ayache. Toward patient-specific myocardial models of the heart. *Heart Failure Clinics*, 4(3):289–301, 2008.

[90] J. Sethian et al. *Level set methods and fast marching methods*. Cambridge university press Cambridge, 1999.

[91] F. Sheehan, S. Ge, G. Vick III, K. Urnes, W. Kerwin, E. Bolson, T. Chung, J. Kovalchin, D. Sahn, M. Jerosch-Herold, et al. Three-Dimensional Shape Analysis of Right Ventricular Remodeling in Repaired Tetralogy of Fallot. *The American Journal of Cardiology*, 2007.

[92] P. Shi and H. Liu. Stochastic finite element framework for simultaneous estimation of cardiac kinematic functions and material parameters. *Medical Image Analysis*, 7(4):445–464, 2003.

[93] P. Y. Simard and G. E. Mailloux. A projection operator for the restoration of divergence-free vector fields. *IEEE Transactions on Pattern Analysis and Machine Intelligence*, 10(2):248–256, 1988.

[94] N. Stergiopulos, B. Westerhof, and N. Westerhof. Total arterial inertance as the fourth element of the windkessel model. *American Journal of Physiology- Heart and Circulatory Physiology*, 276(1):81–88, 1999.

[95] D. Streeter. Gross morphology and fiber geometry of the heart. *Handbook of physiology*, 1:61–112, 1979.

[96] K. Ten Tusscher, D. Noble, P. Noble, and A. Panfilov. A model for human ventricular tissue. *American Journal of Physiology- Heart and Circulatory Physiology*, 286(4):H1573, 2004.

[97] A. Teske, B. De Boeck, P. Melman, G. Sieswerda, P. Doevendans, and M. Cramer. Echocardiographic quantification of myocardial function using tissue deformation imaging, a guide to image acquisition and analysis using tissue doppler and speckle tracking. *Cardiovascular Ultrasound*, 5:27, 2007.

[98] J. Therrien, Y. Provost, N. Merchant, W. Williams, J. Colman, and G. Webb. Optimal timing for pulmonary valve replacement in adults after tetralogy of Fallot repair. *The American journal of cardiology*, 95(6):779–782, 2005.

[99] J. Therrien, S. Siu, P. McLaughlin, P. Liu, W. Williams, and G. Webb. Pulmonary valve replacement in adults late after repair of tetralogy of Fallot: are we operating too late? *Journal of the American College of Cardiology*, 36(5):1670–1675, 2000.

[100] N. Toussaint, T. Mansi, H. Delingette, N. Ayache, and M. Sermesant. An Integrated Platform for Dynamic Cardiac Simulation and Image Processing: Application to Personalised Tetralogy of Fallot Simulation. In *Proc. Eurographics Workshop on Visual Computing for Biomedicine (VCBM)*, Delft, The Netherlands, 2008.

[101] M. Vaillant and J. Glaunes. Surface matching via currents. In *Proc. IPMI 2005*, page 381. Springer, 2005.

[102] T. Vercauteren, X. Pennec, A. Perchant, and N. Ayache. Symmetric log-domain diffeomorphic registration: A demons-based approach. In *Medical Image Computing and Computer Assisted Intervention (MICCAI)*, volume 5241 of *Lecture Notes in Computer Science*, pages 754–761, New York, USA, September 2008. Springer-Verlag.

[103] T. Vercauteren, X. Pennec, A. Perchant, and N. Ayache. Diffeomorphic demons: Efficient non-parametric image registration. *NeuroImage*, 45(1S1):61–72, 2009.

[104] A. Veress, G. Gullberg, and J. Weiss. Measurement of Strain in the Left Ventricle during Diastole with cine-MRI and Deformable Image Registration. *Journal of Biomechanical Engineering*, 127:1195, 2005.

[105] Y. Wang, B. Georgescu, D. Comaniciu, and H. Houle. Learning-based 3D myocardial motion flowestimation using high frame rate volumetric ultrasound data. In *Biomedical Imaging: From Nano to Macro, 2010 IEEE International Symposium on*, pages 1097–1100. IEEE, 2010.

[106] N. Westerhof, J. Lankhaar, and B. Westerhof. The arterial windkessel. *Medical and Biological Engineering and Computing*, 47(2):131–141, 2009.

[107] C. Yang, D. Tang, T. Geva, and P. del Nido. Mri-based patient-specific computational modeling of right ventricular response to pulmonary valve insertion surgery: a passive anisotropic fsi model with fiber orientationspecific computational modeling of

right ventricular response to pulmonary valve insertion surgery: a passive anisotropic fsi model with fiber orientation. In *International Conference on BioMedical Engineering and Informatics*, 2008.

[108] E. Zerhouni, D. Parish, W. Rogers, A. Yang, and E. Shapiro. Human heart: tagging with MR imaging–a method for noninvasive assessment of myocardial motion. *Radiology*, 169(1):59–63, 1988.

[109] H. Zhang, A. Wahle, R. Johnson, T. Scholz, and M. Sonka. 4D Cardiac MR Image Analysis: Left and Right Ventricular Morphology and Function. *IEEE Transactions on Medical Imaging*, 29(2):350–364, February 2010.

[110] Y. Zheng, A. Barbu, B. Georgescu, M. Scheuering, and D. Comaniciu. Four-chamber heart modeling and automatic segmentation for 3-D cardiac CT volumes using marginal space learning and steerable features. *IEEE Transactions on Medical Imaging*, 27(11):1668–1681, 2008.

[111] Y. Zhu, X. Papademetris, A. Sinusas, and J. Duncan. A coupled deformable model for tracking myocardial borders from real-time echocardiography using an incompressibility constraint. *Medical Image Analysis*, 2010.